

Wavelet-based Scale Saliency

Anh Cat Le Ngo^{a,b}, Kenneth Li-Minn Ang^c, Guoping Qiu^b, Jasmine Kah
Phooi Seng^d

^a*School of Electronic Electrical Engineering, The University of Nottingham, Malaysia
Campus*

^b*School of Computer Science, The University of Nottingham, UK Campus*

^c*Centre for Communications Engineering Research, Edith Cowan University*

^d*Department of Computer Science & Networked System, Sunway University*

Abstract

Both pixel-based scale saliency (PSS) and basis project methods focus on multiscale analysis of data content and structure. Their theoretical relations and practical combination are previously discussed. However, no models have ever been proposed for calculating scale saliency on basis-projected descriptors since then. This paper extend those ideas into mathematical models and implement them in the wavelet-based scale saliency (WSS). While PSS uses pixel-value descriptors, WSS treats wavelet sub-bands as basis descriptors. The paper discusses different wavelet descriptors: discrete wavelet transform (DWT), wavelet packet transform (DWPT), quaternion wavelet transform (QWT) and best basis quaternion wavelet packet transform (QWPTBB). WSS saliency maps of different descriptors are generated and compared against other saliency methods by both quantitative and qualitative methods. Quantitative results, ROC curves, AUC values and NSS values are collected from simulations on Bruce and Kootstra image databases with human eye-tracking data as ground-truth. Furthermore, qualitative visual results of saliency maps are analyzed and compared against each other as well as eye-tracking data inclusive in the databases.

Keywords: visual attention, visual saliency, scale saliency, discrete wavelet transform, quaternion wavelet transform, wavelet packet best basis

1. Introduction

A few centuries ago, Neisser proposed a fundamental theory about the human visual attention system including pre-attentive and attentive stages

15 [1] in his psychology studies. However, his work was unknown to machine vi-
16 sion scientists until David Marr [2], a neurologist, proposed a neurology-based
17 computational model for Neisser’s theory. The computational model includes
18 a feature extraction stage followed by perceptual grouping stage. Though the
19 model was practically limited and rarely implemented, it inspires and pro-
20 vides framework for several later computational models. Among them, Itti
21 model [3] holds significant influence and provides a standard in the research
22 field. Itti models feature extraction as center-surrounds operator, a prop-
23 erty of visual cortex; while, perceptual grouping and attentive region assess-
24 ment are due to Proto-Object generation [4] and Winner-Take-All network
25 [3]. After center-surrounds operations in multi-scale levels were proposed for
26 construction of conspicuity and saliency maps by Itti *et al*, other theories
27 like Graph-based Visual Saliency [5], and Spectral Residual Saliency [6] were
28 brought in to produce more meaningful saliency maps [5] as well as reduce
29 the computational complexity [6]. These saliency models assume that human
30 vision systems may behave like random-walk processes [5] or follow statistical
31 property of natural images [5].

32 Without making such strong assumption, Kadir [7] and Gilles [8] initi-
33 ated information-based saliency map with their work on pixel-based scale
34 saliency (PSS). Other information-related saliency research rapidly gained
35 pace with Niel Bruce’s An Information Maximization (AIM) theory [9] and
36 Danash Gao’s Discriminative Information Saliency (DIS) [10]. Furthermore,
37 the information-based spatial-temporal framework (ENT) [11] [12] extends
38 and fastens the models from still images to the dynamic video context.

39 Information-based saliency approaches all motivated from the assump-
40 tion that human attention could be attracted to spatial location accompa-
41 nied with highly informative content. From signal coding, compression and
42 self-information theory, an event has more information when it appears to be
43 structural and rare. Though based on similar concepts, each method has its
44 own information estimation approach on different type of descriptors. Gen-
45 erally, those approaches can be characterized according to their choices of
46 descriptors and calculation methods. For examples, PSS [7] and ENT [12]
47 utilize pixel-value descriptors; meanwhile, AIM [9] and DIS [10] emphasizes
48 on the alternative basis-projection descriptors, ICA bases and Wavelet bases
49 consecutively. In accordance with information measurement, ENT and PSS
50 employ the popular Shannon entropy estimated by histogram construction
51 or Parzen kernel. AIM estimates self-information through neural-network
52 training on patches of natural images. Decision-theory based DIS has its

53 discriminative information from classifying descriptors into center or sur-
54 rounds classes. Noteworthy, PSS is so far the only approach accumulating
55 information of both descriptors and their structure. However, PSS employs
56 pixel-value descriptors and isotropic circular sampling, which might hinder its
57 performance in term of accuracy due to failure in extracting popular oriented
58 features in natural images as well as speed due to the curse of dimensionality
59 in information estimation.

60 The limitation of PSS sparked discussion for alternative solutions by
61 Kadir *et al*[7] [13]. Deploying basis-projected descriptors in place of pixel-
62 based descriptors not only boosts practical performance of scale saliency
63 but as well provides deeper theoretical understanding of scale saliency and
64 data multi-scale structural information. Moreover, the extension would make
65 scale saliency the first-ever method capable of using both pixel-value de-
66 scriptors (PSS) and basis-projection descriptors. Wavelet elements are pre-
67 ferred as alternative basis in this paper; therefore, the proposed method is
68 named Wavelet Scale Saliency (WSS). In order to clearly explain extension
69 from pixel-based descriptors to basis-projection descriptor, we organize this
70 paper in following sections. Section 2 gives overview about scale saliency
71 and its main idea. The next section 3 explains the rationale behind usage
72 of time-frequency domain instead of time-domain only for visual saliency;
73 meanwhile, sections 4, 6 elaborates statistical distribution and correlation
74 of time-frequency descriptors. As wavelet is chosen as time-frequency basis,
75 section 5 gives background information about four types of wavelet trans-
76 forms considered in this study: discrete wavelet transform (DWT), discrete
77 best basis wavelet packet transform (DWPTBB) as well as two quaternion
78 wavelet transforms QWT and QWPTBB. Accordingly, there are four time-
79 frequency descriptors representing time-frequency domain slightly different
80 from each other. Moreover, each descriptor depends on a particular mor-
81 phological shape of its own mother wavelet. All details about properties
82 of those descriptors are organized in section 6.1. Along with new descrip-
83 tors, suitable mathematical models of feature-space and inter-scale saliency
84 estimation are derived in section 7. Moreover, the mathematical derivation
85 unveils strong relation between WSS with another state-of-the-art Bayesian
86 Surprise Saliency (BSS) [14]. Beside theoretical evaluation, simulations on
87 Neil Bruce image database [15] and Kootstra image database [16] are carried
88 out in order to compare quantitatively the proposed WSSs with different
89 basis-projection descriptors, the original PSS and the ITT model. Further-
90 more, qualitative analysis on particular images provides better details about

91 responses of the proposed methods with different types of scenes. It is pos-
 92 sible that performance of saliency methods depends on image content. All
 93 results and discussion are detailed in the section 8. Finally, the conclusion 9
 94 summarizes our main contributions and future research directions.

95 2. Scale Saliency

96 To get a hold of what exactly is a scale saliency; a few fundamental princi-
 97 ples of original scales saliency are reviewed. Scale saliency utilizes maximum
 98 feature-space entropy weighted by its inter-scale dependency across scales as
 99 saliency values; furthermore, it argues that information measurement might
 100 be data-driven pivot for human visual attention. Its mathematical model is
 101 summarized as follows.

$$Y_D(s_p, \vec{x}) = H_D(s_p, \vec{x}) W_D(s_p, \vec{x}) \quad (1)$$

$$H_D(s_p, \vec{x}) = - \int_{d \in D} p(d, s_p, \vec{x}) \log_2(p(d, s_p, \vec{x})) dd \quad (2)$$

$$W_D(s_p, \vec{x}) = s \int_{d \in D} \left| \frac{\delta p(d, s_p, \vec{x})}{\delta s} \right| dd \quad (3)$$

$$s_p = \left\{ s \left| \frac{\delta H_D(s, \vec{x})}{\delta s} = 0; \frac{\delta^2 H_D(s, \vec{x})}{\delta s^2} < 0 \right. \right\} \quad (4)$$

102 Feature-space saliency, (H_D) in the equation 2, is measured by its Shannon
 103 entropy of pixel-values descriptor (d) at a specific scale or sampling window
 104 size (s) for each image location (\vec{x}). Shannon entropy is chosen since it
 105 satisfies four over five criteria of multi-scale entropy filtering [17]. The last
 106 criterion actually requires structural correlation from information estimation,
 107 which is apparently not considered in Shannon entropy. However, inter-
 108 scale saliency, (W_D), actually fulfils this requirement, and it is estimated
 109 at every location by total variation of descriptors' probability distribution
 110 function (*PDF*) across scales. Then, the scale (s_p) at which most significant
 111 information should be found; it is actually the maximum point of the scale-
 112 entropy concave curve in the equation 4. Finally, the overall saliency is
 113 stated mathematically as the equation 1 in accordance with the definition
 114 of scale saliency. Lets apply the concept of scale saliency on a general form
 115 of signal $R(x_0, s_i) = \{I(\vec{x}_0, s_i) + N(\vec{x}_0, s_i) | i = 1..n\}$, where $I_{\vec{x}_0, s_i}$ is ideal
 116 noise free signal, $R_{\vec{x}_0, s_i}$ is the measured signal with noise $N_{\vec{x}_0, s_i}$ at specific
 117 location and scale (\vec{x}_0, s_i). Assumed no dependencies between noise and the

118 ideal signal, the estimated entropy is $H_D(R_{\vec{x}_0, s_i}) = H_D(I_{\vec{x}_0, s_i}) + H_D(N_{\vec{x}_0, s_i})$.
 119 Assumed that noise *PDF* are scale-invariant, the equation 3 implies that
 120 inter-scale saliency measure is purely dependent on variation of useful signal
 121 $\Delta_{s_i} H_D(I_{\vec{x}_0, s_i})$ and not affected by variation of noise $\Delta_{s_i} H_D(N_{\vec{x}_0, s_i}) = 0$.
 122 This briefly explains basic motivation behind scale saliency work; further
 123 mathematical analysis and experiments results can be found in [7] [13].

124 The original scale saliency [7] uses pixel-value descriptors which are sim-
 125 ple, intuitive, and straight forward interpretation of image data. Moreover,
 126 its combination with circular sampling window provides isotropic informa-
 127 tion analysis, independent of any morphological shape inside sampled re-
 128 gions. Nevertheless, its drawbacks are be susceptible to noise, require high
 129 computational cost and cause significant bias in entropy estimation. So far,
 130 histogram construction and approximated Parzel kernel are two popular pa-
 131 rameter methods for constructing pixel-value descriptors' *PDF* and esti-
 132 mating entropy. Entropy bias and speed performance in those mentioned
 133 methods greatly depend on manual tuning of histogram numbers of bins or
 134 Parzel size kernel; in addition, they as well restrict extension of scale saliency
 135 to higher dimensional data. Suau [18] overcomes these problems by bypass-
 136 ing *pdf* construction stage and estimating PSS by multivariate-data-adaptive
 137 information estimation technique [19]. In spite of its fast computation for
 138 multivariate data, the non-pdf approach hinders the inter-scale saliency pro-
 139 cess which directly depends on *PDF*s 3. It is solved by adapting set-theory
 140 based elegant solutions of Kadir [13] for inter-scale saliency W_D computation
 141 into kd-tree structure. However, the solution is not intuitively and mathe-
 142 matically related to the information-based frame-work. That motivates us
 143 develop (*WSS*), a more coherent information-based scale saliency with sub-
 144 band energy descriptors, as solutions for all these short-comings of PSS.

145 3. Time-Scale-Frequency

146 A well-known computational model of visual attention is first mentioned
 147 in Koch and Ullman's publication [20]. After that, several other models are
 148 proposed; however, they are usually over-complex and not biologically plau-
 149 sible. The disadvantages might be due to pixel representation utilized in
 150 many early visual attention algorithm. To overcome these problems system-
 151 atically, Urban [21] has investigated strong constraints to keep computational
 152 complexity within an acceptable range for possible real-time implementa-
 153 tion. These constrains are drawn from evidences of psychological experiments

Depth	0	1	2	3	4	5
Frequency range (cycles per degree)	10.7-5.3	5.3-2.7	2.7-1.3	1.3-0.7	0.7-0.3	0.3-0.2

Table 1: Wavelet Levels vs Frequency Range

154 which shows that images could be analyzed in psycho-visual channels at least
 155 in TV-viewing condition [22]. In other words, visual data could be further
 156 analysed into channels and sub-bands instead of being used in raw pixel
 157 format. Furthermore, the channels can be effectively characterized by sepa-
 158 rated frequency bands and orientation ranges of wavelet analysis [23]. Lets
 159 assume visual active areas of brains can deploy some 9/7 Cohen-Daubechies-
 160 Feauveau (CDF) wavelet transform operators; then, it results in multi-scale
 161 pyramid composed of oriented contrast maps with limited frequency range
 162 and low-resolution image. For each level of wavelet decomposition, there are
 163 four channels: (i) sub-band 0 is approximated image after filtered with many
 164 low-pass blurring kernels; (ii) sub-band 1 extracts horizontal frequencies cor-
 165 responding to vertical edges of images (iii) sub-band 2 contains frequencies
 166 and features along two diagonals of image frames. (iv) sub-band 3 prefers ver-
 167 tical frequencies mapping to horizontal features form images. Natural scenes
 168 are full of horizontal, vertical or two diagonals features; therefore, human
 169 visual perception seems to prefer those dominant features. Besides oriental
 170 constraints, visual acuity is another visually perceptual limit. Normally, hu-
 171 man fovea could decompose and process details above its limit visual acuity
 172 (1.5-2 degrees of visual angle). It lasts in frequency range: 0.7-0.5 pixels per
 173 degree, or 0.33-0.25 cycles per degree. This range is nearly resembled by the
 174 last level low-resolution version of images in usual wavelet decomposition.
 175 Each decomposed level are generated by moving kernels with different win-
 176 dow size to any image positions. Spatial frequency of other wavelet analysis
 177 levels, varying in accordance with analyzing depths, is shown the following
 178 table 1

179 Spectral energy are usually employed as spectral signature for image col-
 180 lections or individual images. Urban *et al*[21] analyses different sets of images
 181 belonging to four different semantic categories: coast, mountain, street and
 182 open-country. Interestingly, Fourier spectrum of each category possess dis-
 183 tinguished shape and frequency range, significantly different from each other
 184 [21]. In other words, each general spectral profile and associated distribution
 185 histogram of image classes have unique energy distribution. This distribution

186 is proportional to distance d from mean magnitude spectrum normalized by
 187 the standard deviation of the category.

$$d(s) = \frac{1}{nm} \sum_{n,m} |s(n, m) - AS(n, m)|$$

188 where $AS(n, m)$ is average spectrum. Carefully observing the spectral pro-
 189 files could give distinguishing clues for each semantic scene. For example,
 190 "Coastal" scenes are dominated with horizontal features; therefore, its spec-
 191 tral profiles stretch along vertical axes. Furthermore, spectral profile of
 192 "OpenCountry" categories is biased toward two upper and lower spectrum.
 193 Though almost similar to the "OpenCountry" profile, spectrum of "Street"
 194 images includes more types of features from artificial environment beside
 195 horizon-oriented details. Therefore, the diamond of image spectral profile of
 196 "Street" becomes more significant horizontally. "Mountain" categories with
 197 its random scenic details have isotropic spectrum while scenes of streets filled
 198 with artificial objects have spectrum stretched in both horizontal and ver-
 199 tical axis. From Urban's research, spectral energy distribution seems to be
 200 important clues for visually perceptual system of human beings.

201 Beside image classification, the spectral distribution signature is as well
 202 useful in visual attention and early visual process. Such energy distribution
 203 becomes differentiable clues for features across scales. Spectral profiles of
 204 image feature at a particular scale would help differentiate itself from directly
 205 upper and lower scale. Lets do an imaginary experiments with a single square
 206 input signal $x(t)$ defined as follows.

$$x(t) = \begin{cases} 1 & t_1 \leq t \leq t_2 \\ 0 & t < t_1 \vee t > t_2 \end{cases}$$

207 If $x(t)$ is filtered by a kernel $F()$ with kernel size (1-D kernel width)
 208 $W = \Delta T$ and W is much smaller than non-zero period of the given square
 209 signal $\Delta T \lll |t_2 - t_1|$, the response will be just two impulse function at
 210 t_1, t_2 .

$$F(x(t)) = \begin{cases} 1 & t = t_1 \wedge t = t_2 \\ 0 & t \neq t_1 \vee t \neq t_2 \end{cases}$$

211 For 2-D signal or image context, the above operation corresponds to a classic
 212 edge detection phenomena. Though edges and structures plays important

213 roles in visual perception, their information does not sufficiently represent
 214 the whole natural scenes. Natural images are rich of other features like tex-
 215 ture, flat regions, etc beside edges and corners. As mentioned before, image
 216 features can be interpreted in terms of energy distribution. For example,
 217 edges are the places of high energy concentration, homogeneous flat regions
 218 do not contain much energy while textures, hybrid of edges and flat regions,
 219 contains certain amount of energy . If only one window size is used in the
 220 analysis, significant responses only come from features or objects which hap-
 221 pen to fit into that window size. The other useful features with inappropriate
 222 size in accordance with the filter could not be extracted. Therefore, a multi-
 223 scale’s approach is extremely necessary in order to identify suitable sizes of
 224 kernels or fuse features from different scales together. When mother wavelet
 225 is chosen as filtering kernels, window size becomes equivalent to frequency
 226 range in the table 1, and choosing adaptive frequency ranges is important
 227 computation task for spatial feature extraction. Inspired by such fundamen-
 228 tal query in computer vision, this paper tries to contribute a little insight
 229 about how spectral density distribution can characterize features at each
 230 scale and how the frequency range of processing can be appropriately cho-
 231 sen for multi-scale feature representation. From the multi-scale features and
 232 appropriate scale selection, we can develop computation saliency methods
 233 capable of highlighting salient features across scales by using spectral energy
 234 distribution.

235 4. Time-Scale-Energy

236 PSS estimates information from pixel values, time-domain descriptors by
 237 constructing normalized histogram of pixel values as probability distribution.

$$p_h(d) = \frac{n_d}{N}$$

238 where p_h is probability of descriptor, the ratio between number of pixels with
 239 d descriptors and total image pixels N . Lets use square of pixel d^2 as weights

$$p_e(d) = \frac{n_d * d^2}{\sum_D (n_d * d^2)} = \frac{\rho_x}{E_x} = \frac{\int_{-\infty}^{\infty} (x(t)\delta(x(t) - d))^2 dt}{\int_{-\infty}^{\infty} x(t)^2 dt}$$

240 Normalized weighted-histogram $p_e(d)$, of signal $x(t) \in L^2(R)$ can obviously
 241 be interpreted as ρ_x energy density of descriptors d in time domain. By
 242 the isometric property of the Fourier transform, the *PDF* of energy density
 243 distribution can be expressed in frequency domain as well.

$$p_e(\hat{d}) = \frac{\rho_{\hat{x}}}{E_{\hat{x}}} = \frac{\int_{-\infty}^{\infty} \hat{x}(f)^2 \delta(\hat{x}(f) - \hat{d}) df}{\int_{-\infty}^{\infty} \hat{x}(f)^2 df}$$

244 Or in joint time and frequency domain.

$$p_e = \frac{\rho_{\bar{x}}}{E_{\rho_{\bar{x}}}} = \frac{\rho_{\bar{x}}(t, f)}{\int_{-\infty}^{\infty} \int_{-\infty}^{\infty} \rho_{\bar{x}}(t, f) dt df}$$

245 where

$$\rho_{\bar{x}} = \left| \int_{-\infty}^{\infty} x(\tau) g_{t,f}^*(\tau) d\tau \right|^2$$

246 where $\rho_{\bar{x}}$ is energy density in joint time-frequency representation. Pure time
 247 descriptors have perfect localization in time, no localization in frequency ,
 248 and vice versa for frequency descriptors. Both extreme time or frequency
 249 descriptors make interpretation of constructed *PDF*, and estimated infor-
 250 mation difficult to explain. Therefore, it is necessary to find a representa-
 251 tion of $g_{t,f}^*(\tau)$ which describes spectral density of local energy. For example,
 252 Short-Time Fourier Transform (STFT) is the first-known transform capable
 253 of generating spectrogram, a graphical representation of local signal energy
 254 in time-frequency plan.

$$\rho_x(t, f) = \left| \int_{-\infty}^{\infty} x(\tau) h^*(\tau - t) e^{-2j\pi f\tau} d\tau \right|^2$$

255 STFT identifies spectral density as well as local energy density or infor-
 256 mation in a short-time period of the signals. However, it does not much
 257 benefit scale saliency unless scale parameters are actually considered as in
 258 signal description on phase-space. Fortunately, in recent years, alternative
 259 scale-based representation, called wavelet-transform (WT), has been widely

260 addressed among signal processing community, and its fundamental idea is
 261 replacing the frequency shifting operation $e^{-2j\pi f\tau}$ by a time (or frequency)
 262 scaling operation $\psi(\frac{t-\tau}{a})$, a basic wavelet kernel. Consequently, the energy
 263 density in WT framework is formulated as follows.

$$\rho_x(t, a) = \left| \int_{-\infty}^{\infty} x(\tau) \psi\left(\frac{\tau - t}{a}\right) d\tau \right|^2$$

264 WT coefficients, $\rho_x(t, f)$, averagely measure spectral density of frequency
 265 sub-bands, a short range of frequency, in a short period of time. Character-
 266 istics of the time-frequency window are specified by two main parameters,
 267 time-shift τ and scale a . As derived from short-time spectral representation,
 268 a spectrogram, by utilizing scale operations, its energy density distribution
 269 is called scalogram. Given time-scale space, the total signal energy can be
 270 rewritten as follows.

$$E_{\rho_x} = \int_{-\infty}^{\infty} \int_{-\infty}^{\infty} \rho_x(t, a) dt da$$

271 and probability of time-scale descriptors can be specified with scale param-
 272 eters

$$P_e(t, a) = \frac{\rho(t, a)}{E_{\rho_x}} \quad (5)$$

273 Generally, the wavelet transform can help generate frequency sub-band co-
 274 efficients, square of which over total energy are density distribution of that
 275 sub-band in time-scale space.

276 5. Wavelet Transform

277 After discussing about usefulness of time-frequency-scale representation
 278 in the section 3 and its corresponding time-frequency energy distribution,
 279 we recognize that wavelet-representation would be ideal candidates for our
 280 investigation into energy density distribution and other statistical property
 281 across multiple scales of natural images. During the quite short history of
 282 wavelet analysis, this research fields have been very fruitful and there are sev-
 283 eral analysing techniques with wide range of characteristics. In this paper,
 284 only standard techniques such as discrete wavelet transform (DWT), dis-
 285 crete wavelet packet transform (DWPT), quaternion wavelet transform with

286 best-basis(QWTBB), and quaternion wavelet packet transform with best-
287 basis. are deployed as possible descriptors. In this subsection, we first look
288 into discrete and real wavelet and wavelet packet transform with best basis
289 (DWT,DWPTPP) for its theoretical background; then QWT and QWPTBB,
290 quaternion versions of two prior wavelet transforms, are considered.

291 *5.1. Discrete Wavelet Transform*

292 Though wavelets were firstly introduced in the early 20th century by
293 Alfred Harr, they are only developed rapidly much later. Only until recently,
294 they have been widely employed in many computer vision problems such as
295 image or video de-noising, enhancement, coding, and pattern classification
296 [24, 25, 26] . Signal analysis for frequency components can be achieved
297 by Fourier transform (FT) but FT does not provide suitable tool for time-
298 frequency analysis of images. Short-time Fourier Transform (STFT) is an
299 extension from FT approach for analysing local frequency analysis at a short
300 period of time [27]. Noteworthy that, STFT can be used for taking the spatial
301 interval in 2-D signal instead of time period in 1-D type since there is no time
302 dimension for still images. However, STFT utilizes fixed window kernels for
303 every data blocks across input signals; this property make STFT less suitable
304 for complex signal analysis, especially signals with strong semantic structures
305 appearing across multiple scales. In other words, STFT only succeeds with
306 signals whose features are embedded in fixed definite temporal or spatial
307 regions or there is prior knowledge about a suitable size of window kernel for
308 STFT processing. Without the above conditions, STFT would totally miss
309 signal features. Theoretically, the disadvantage can be avoided by employing
310 STFT with multiple kernel sizes; however, it raises up another issues such
311 as what range of sizes would be chosen to optimally extract useful features
312 with reasonably computational effort.

313 Problems of STFT in analyzing local frequency have motivated develop-
314 ment of multi-scale wavelet techniques for better local frequency represen-
315 tation. Since limitations of STFT is due to fixed-size processing windows,
316 wavelet analysis deploys multi-resolution filter-banks on input signals. As il-
317 lustrated in figure 1, 1-D signals are decomposed into low-pass and high-pass
318 components. In case of 2-D input signals, the filtered outputs are four sub-
319 bands: low-low, high-low, low-high, and high-high in regards of processing
320 orientation. Intuitively, 2-D signals analysis includes row-wise 1-D analysis
321 followed by column-wise 1-D analysis or vice verse. With respect to process-
322 ing direction, high-low sub-band tends to extract horizontal features, low-

323 high sub-band prefers vertical features, high-high sub-band detects diagonal
 324 features, and low-low are approximated version of original signal by inverse
 325 dyadic scale. Lets assume that input signals are two-dimensional grey-scale
 326 image $f(x, y)$, and the scaled mother wavelets have following mathematical
 327 form $\psi_{s,i}(x, y) = 2^s \psi(2^s x, 2^s y)|_{i=\{v,h,d\}}$ for vertical, horizontal and diagonal
 328 sub-bands and a scaling function $\phi_S(x, y) = 2^S \phi(2^S x, 2^S y)$ for low-resolution
 329 signals with $s \geq S$. Then, we can represent any images $f(x, y) \in L_2(\mathbb{R})$ as.

$$f(x, y) = \sum_{x,y} c_S(x, y) \phi_S(x, y) + \sum_{i=\{v,h,d\}} \sum_{x,y,s \geq S} d_{s,i}(x, y) \psi_{s,i}(x, y)$$

330 where

$$c_S(x, y) = \int f(x, y) \phi_S(x, y) dx dy$$

331

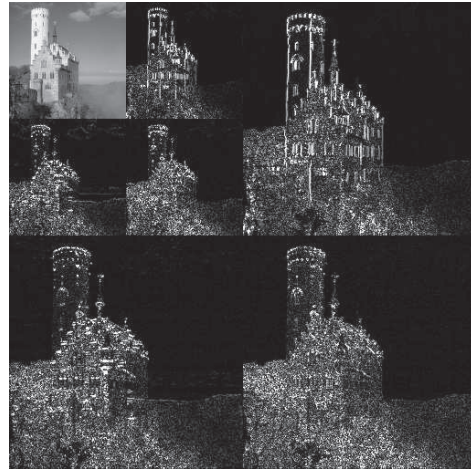
$$d_{s,i}(x, y)|_{i=\{v,h,d\}} = \int f(x, y) \psi_{s,i}(x, y) dx dy$$

332 $c_S(x, y)$ and $d_{s,i}(x, y)$ are scaling coefficients and wavelet coefficients from
 333 vertical, horizontal and diagonal sub-bands. The parameter S represents the
 334 lowest analyzing depth while s is higher decomposing levels in multiple scale-
 335 space framework. As mentioned before, 2-D DWT can be obtained by tensors
 336 products of 1-D DWT when the original image $f(x, y)$ is analyzed along two
 337 dimensions x and y separately. As a result, the scale function $\phi(x, y)$ is
 338 approximated as $\phi(x)\phi(y)$ and filter-banks of three directional sub-bands are
 339 $\phi(x)\psi(y)$, $\psi(x)\phi(y)$, $\psi(x)\psi(y)$. In the figure 1, discrete wavelet transforms
 340 are carried on the sample image in the left hand-side. On the right-hand side
 341 contains decomposed results by two levels with three distinctive sub-bands
 342 and a down-sampled version of the original image.

343 Noteworthy that, the real-wavelet transform like DWT suffers from shift-
 344 variance, a small shift in the signal can greatly change magnitudes of wavelet
 345 coefficients around singularities. Furthermore, it has no phase to embed sig-
 346 nal location information therefore aliasing effects would be introduced into
 347 recovery process. These issues need seriously considering whenever the dis-
 348 crete real wavelet transform is employed. Therefore, modelling statistical
 349 property of DWT coefficients' magnitude across scales might request extra
 350 investigation with those draw-backs in mind. Further arguments and details
 351 about this matter of DWT descriptors will be discussed in the section 2.



(a) Sample Image



(b) Wavelet Decomposition

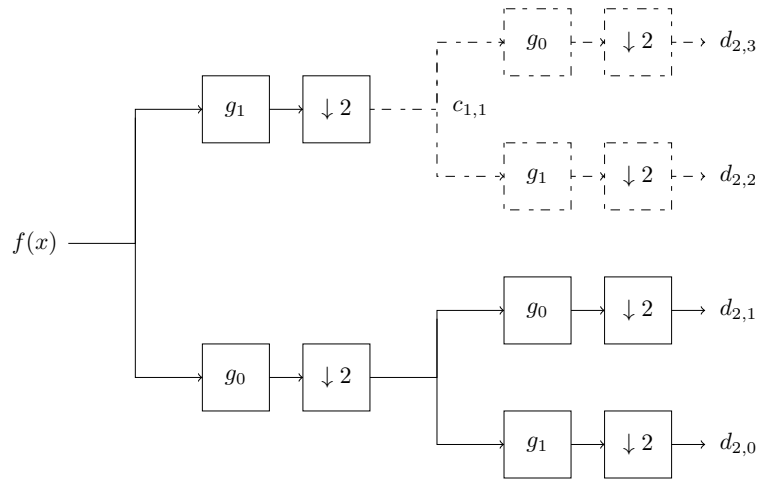


Figure 1: Wavelet (solid line) & Wavelet Packet Decomposition (solid and dash lines) for 1-D signal

352 *5.2. Discrete Wavelet Packet Transform*

353 Well-known DWT can be computed efficiently by an orthonormal FIR
 354 conjugate quadrature filter banks g_0, g_1 including analysis low-pass and high-
 355 pass filters (denoted ϕ_S and $\psi_{s,i}$ respectively. The low-pass coefficients
 356 $c_S(x, y)$ are decomposed recursively for a number of levels, and inverse dis-
 357 crete wavelet transform is calculated by an inverse filter bank. The exten-
 358 sion from normal wavelet transform (DWT) to wavelet packets transform
 359 (DWPT) is straightforward by an additional step at each processing level.
 360 Instead of decomposing only low-pass coefficients in the Low-Low sub-band
 361 for 2D input signals, the transform performs decomposition of high-pass co-
 362 efficients in Low-High, High-Low and High-High sub-bands as well. As a
 363 result, all coefficients of DWPT can be neatly arranged in a binary tree and
 364 addressed as follows.

$$d_{s,i}(x, y) , s \in [0, S], i \in [0, 4^s - 1]$$

365 where s is a analysis depth in the tree, S notes the deepest decomposed level,
 366 and i is the node index in this depth. With regards to other representations,
 367 wavelet packets have advantages in their adaptability to varying statisti-
 368 cal structure. Unlike Fourier Transform with one fixed-size base or normal
 369 wavelet transform with a fixed number of bases, we may search the “best”
 370 orthonormal bases from dictionary of basis acquired after wavelet package de-
 371 composition. This idea is initially proposed by Coifman *et al*[28] mainly for
 372 signal compression. Therefore, this “best” basis is the best in terms of com-
 373 pressing ratio which often desires sparsest representation. In other words,
 374 input signals can be characterized by few large coefficients. Supposed the
 375 whole best basis operation is denoted as B^2 which exhaustively goes through
 376 the whole binary tree to look for locations of a set basis with parameters
 377 (\mathbf{s}, \mathbf{i}) such that the there is a minimum amount of uncertainty measured by
 378 Shannon entropy. More details can be found in Coifman’s works [28], and
 379 B^2 can be summarized mathematically as follows.

$$B^2(d_{s,i}) : (\mathbf{s}, \mathbf{i}) = argmin_{s,i} (\sum H(d_{s,i}))$$

380 Noteworthy that, sometime “brute-force-attack” every branch of the tree is
 381 not possible or feasible due to intensive requirement of computational power.
 382 Fortunately, there exist fast algorithms to implement the best basis for given
 383 signals. Then, the optimum time-frequency representation can be achieved

384 by tilting the time-frequency plan in accordance with best-basis algorithms.
385 Though the representation may be optimally sparsest in time-frequency do-
386 main, whether sparseness of features suitably matches performance of human
387 visual attention is still a question to be answered. To rectify the matter, ex-
388 periments have been carried out and performance comparison between the
389 DWT case and DWPTBB case is reported in the section 8.

390 5.3. Quaternion Wavelet Transform

391 Like wavelet packet transform in the previous discussion, Quaternion
392 Wavelet Transform (QWT) is extended and enhanced to eliminate shift-
393 variance problems from real discrete wavelet transform (DWT). Though there
394 are a few different definitions and implementations of Quaternion Wavelet
395 [29], the QWT implementation in this paper is inspired by Chan’s research *et*
396 *al*[26]. Some backgrounds about complex wavelet transform (CWT) with its
397 implementation dual-tree complex wavelet transform (DT-CWT) Kingsbury
398 *et al*[30] need reviewing before the QWT can be explained and discussed. In
399 discrete wavelet transform, 2-D DWT can be considered as concatenation of
400 two consecutive 1-D DWTs. Though the same process does not exactly hap-
401 pen in 2-D DT-CWT or QWT straightforwardly. A similar concept is used
402 for easily explaining how QWT can be achieved. It means 1-D DT-CWT will
403 be elaborated first; then, we will discuss about 2-D QWT signals and how it
404 may handle processing along different orientations and sub-bands.

405 Real DWT have well-known drawbacks in terms of shift-invariance and
406 phases to encode coefficient locations. Kingsbury *et al*[31] reckons problems
407 and proposes an dual-tree CWT as a specific solution. Rationale of the dual-
408 tree approach is usage of complex numbers for wavelet coefficients which
409 directly tackles one of two DWT’s dragging problems. Complex extension of
410 wavelet transform makes phase extraction from wavelet coefficients possible
411 since complex wavelet transforms have both real and imaginary values unlike
412 real DWT with only one real value for each coefficient. Real and imaginary
413 components of the dual-tree CWT are generated by two sets of wavelet and
414 scaling functions ψ_h, ψ_g and ϕ_h, ϕ_g . Moreover, filter-banks h_0, h_1 and g_0, g_1
415 have to be independent and orthogonal as shown in the figure 2.

416 The notations $\phi_h(x)$ and $\psi_h(x)$ are denoted for scaling and wavelet func-
417 tions corresponding to filter-banks h_0, h_1 . In addition, c_{h_s} and d_{h_s} with $s \leq S$
418 denotes first set of DTCWT coefficients. Similar notations are used for the
419 second set of scaling and wavelet functions $\phi_g(x)$ and $\psi_g(x)$ with filter banks
420 g_0, g_1 and according coefficients c_{g_s} and d_{g_s} with $s \leq S$. Wavelet functions

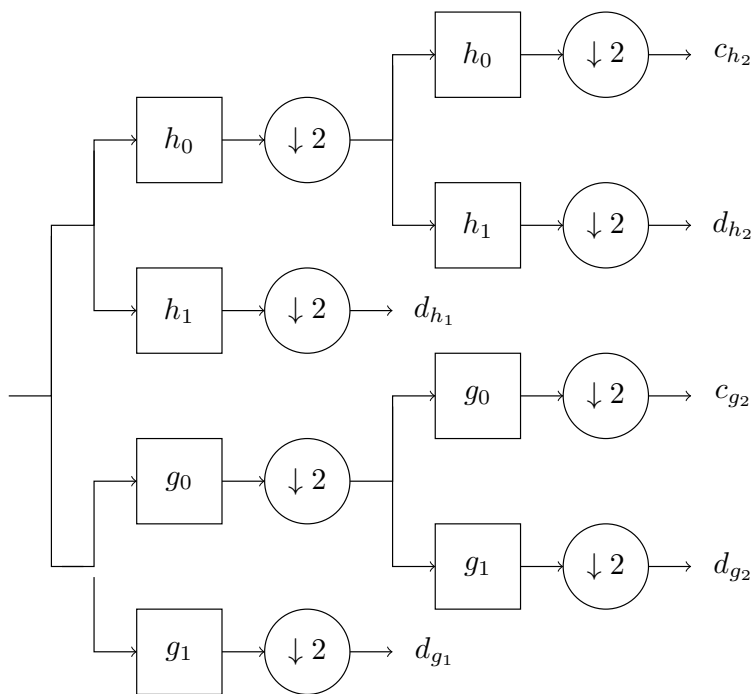


Figure 2: Illustration of DTCWT

421 $\psi_h(x)$ and $\psi_g(x)$ forms two binary trees in figure 2 and at leaves of each tree
 422 is the real and imaginary parts of a complex analytic wavelets.

$$\psi^{(c)}(x) = \psi_h(x) + j\psi_g(x)$$

423 Moreover, the imaginary wavelet $\psi_g(x)$ is 1-D Hilbert Transform of the real-
 424 wavelet $\psi_h(x)$:

$$\psi_g(x) = \mathcal{HT}(\psi_h(x))$$

425 Any complex wavelet coefficient are formed by wavelet coefficients of two
 426 other real wavelet transforms; therefore, this combination generates a 2 x
 427 redundant tight frame. This redundancy in complex wavelet frames prevents
 428 non-oscillating magnitudes of coefficients around singularity points as well
 429 makes the transform near-shift invariant. Furthermore, there is no energy (
 430 or little energy in practice) in the negative region of frequency because of a
 431 relationship between two wavelet functions ψ_h and ψ_g .

$$\Psi_g(\omega) = \begin{cases} -j\Psi_h(\omega) & \omega > 0 \\ j\Psi_h(\omega) & \omega < 0 \end{cases}$$

432 then

$$\begin{aligned} \Psi^c(\omega) &= \mathcal{F}(\Psi^c(x)) \\ &= \mathcal{F}(\Psi_h(x) + j\Psi_g(x)) \\ &= \Psi_h(\omega) + j\Psi_g(\omega) \end{aligned}$$

433 and

$$\Psi^c(\omega) = \begin{cases} 2\Psi_h(\omega) & \omega > 0 \\ 0 & \omega < 0 \end{cases}$$

434 Thus, the Fourier transform of complex wavelet transform $\Psi^c(\omega)$ has no
 435 energy in the negative frequency region. It makes DTCWT an analytic
 436 wavelet transform with analytic output signals. Due to this analyticity, the
 437 dual-tree wavelet transform has implicitly managed to include all information
 438 in the half positive plan of the frequency domain.

439 It is quite straight forward for 2-D DWT expansion from 1-D DWT, dis-
 440 cussion in the previous subsection 5.1. However, it is unfortunately not easy
 441 for similar expansion from 1-D DTCWT to 2-D DTCWT transforms because
 442 Hilbert Transform (HT) and analytic signals need an theoretical extension

443 for 2-D signals. Furthermore, there exists not only one but several defi-
444 nitions which define different zero-out regions (negative frequency domain
445 in 1D DT-CWT) , signal-power regions (positive frequency domain in 2D
446 DT-CWT). In this paper, we only focus on Bulow definition [29] of analytic
447 quaternion signals which combines both partial and total Hilbert transform
448 (HT) . Partial HTs are done along either x or y directions only; meanwhile,
449 total HT is carried out on both directions simultaneously. They are defined
450 as following formula.

$$\begin{aligned} f_{\mathcal{H}_{i_1}}(\mathbf{x}) &= f(\mathbf{x}) \circ \frac{\delta(y)}{\pi x} \\ f_{\mathcal{H}_{i_2}}(\mathbf{x}) &= f(\mathbf{x}) \circ \frac{\delta(y)}{\pi x} \\ f_{\mathcal{H}_i}(\mathbf{x}) &= f(\mathbf{x}) \circ \frac{1}{\pi^2 xy} \end{aligned}$$

451 The $f_{\mathcal{H}_{i_1}}, f_{\mathcal{H}_{i_2}}(\mathbf{x})$ are partially Hilbert transformed along x and y axis
452 consequently, and $f_{\mathcal{H}_i}(\mathbf{x})$ is total HT; while \circ denotes 2-D convolution. Each
453 2-D CWT basis is a complex analytic function, computationally equivalent
454 to a product of two 1-D complex wavelet functions either along only one or
455 both axis. Similar to expansion of discrete real wavelet, the diagonal sub-
456 band wavelet is defined as $f(\mathbf{x}) = \psi_h(x)\psi_h(y)$. Other total and partial HT
457 are products of coefficients from different sets of wavelet functions deployed
458 in the 1-D CWT implementation.

$$(f_{\mathcal{H}_{i_1}}, f_{\mathcal{H}_{i_2}}, f_{\mathcal{H}_i}) = (\psi_g(x)\psi_h(y), \psi_h(x)\psi_g(y), \psi_g(x)\psi_g(y))$$

459 To unify all different Hilbert Transform in a meaningful and compact rep-
460 resentation, we can utilize quaternion algebra and treat $f(\mathbf{x})$ as a real part
461 and $(f_{\mathcal{H}_{i_1}}, f_{\mathcal{H}_{i_2}}, f_{\mathcal{H}_i})$ as three imaginary components [26].

$$f_A^q(\mathbf{x}) = f(\mathbf{x}) + j_1 f_{\mathcal{H}_{i_1}}(\mathbf{x}) + j_2 f_{\mathcal{H}_{i_2}}(\mathbf{x}) + j_3 f_{\mathcal{H}_i}(\mathbf{x})$$

462 More details about theory behind QWT and its special characteristics such as
463 its singular cases, three phases, and zero-out regions can be found in Chan
464 etal 's and Bulow 's publications [26, 29]. Resting on form of the above
465 quaternion wavelet transformation, we can organize four quadrant compo-
466 nents of 2-D wavelet $(f, f_{\mathcal{H}_{i_1}}, f_{\mathcal{H}_{i_2}}, f_{\mathcal{H}_i})$ as a quaternion. Lets take a example
467 of diagonal signals with following quadrant components.

$$(f, f_{\mathcal{H}_{i_1}}, f_{\mathcal{H}_{i_2}}, f_{\mathcal{H}_i}) = (\psi_h(x)\psi_h(y), \psi_g(x)\psi_h(y), \psi_h(x)\psi_g(y), \psi_g(y)\psi_g(y))$$

468 We can have a diagonal quaternion wavelet functions for the diagonal sub-
 469 band mathematically defined as follows.

$$\psi^D(x, y) = \psi_h(x)\psi_h(y) + j_1\psi_g(x)\psi_h(y) + j_2\psi_h(x)\psi_g(y) + j_3\psi_g(x)\psi_g(y)$$

470 To compute the QWT coefficients, we can use proposals of a separable 2-
 471 D implementation [31] of dual-tree filter-banks previously illustrated in the
 472 figure 2. At each filtering stage, both two-sets of wavelet filters h and g are in-
 473 dependently applied to each dimension x and y of a 2-D image. For example,
 474 the filter-bank h is applied along both axis; then, it yields the scaling co-
 475 efficients c_{hh_s} and three diagonal, vertical and horizontal wavelet coefficients
 $d_{hh_s}^D$, $d_{hh_s}^V$ and $d_{hh_s}^H$ respectively as shown in the figure 3. Dual-tree implemen-

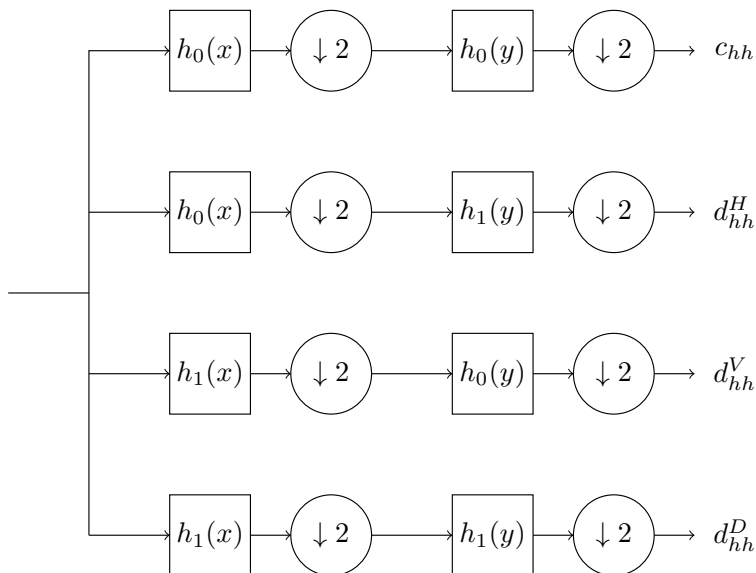


Figure 3: Illustration of 2D dual-tree complex wavelet transform

476 tation of two separated filter-banks for 1-D signal can be considered as four
 477 independent filter banks for 2-D signals according to all possible combina-
 478 tions of filter for one dimension (hh , hg , gh , gg). With these combinations of
 479 filters and corresponding wavelet functions $\psi(x)\phi(y)$, $\phi(x)\psi(y)$ and $\psi(x)\psi(y)$
 480 are generated four components of quaternion wavelet transform for horizontal,
 481 vertical, and diagonal sub-bands. Four different wavelet coefficients from
 482 these filter banks are arranged by quaternion algebra to obtain QWT coef-
 483 ficients. For example, a coefficient from diagonal wavelet sub-band of QWT
 484

485 can be written in terms of responses from independent filter-banks as follows.

$$d_s^D = d_{hh}^D + j_1 d_{gh}^D + j_2 d_{hg}^D + j_3 d_{gg}^D$$

486 So far, we have taken a diagonal sub-band as example for showing how QWT
 487 can be computed. The construction and properties for other two sub-bands
 488 are similar to what have been done for diagonal sub-bands. Except that the
 489 axis combinations results in a horizontal sub-band $\psi(x)\phi(y)$ or for a vertical
 490 sub-band $\psi(x)\psi(y)$ instead of a diagonal sub-band $\psi(x)\psi(y)$. In summary,
 491 QWT at each stage sports three quaternion sets corresponding to three sub-
 492 bands; each quaternion contains four wavelet functions. Therefore, there
 493 are 12 functions in total which can be easily seen as matrix of functions as
 494 follows.

$$\begin{aligned} \left[\begin{array}{ccc} d_s^H & d_s^V & d_s^D \end{array} \right] &\stackrel{q}{=} \begin{bmatrix} d_{hh}^H & d_{hh}^V & d_{hh}^D \\ d_{gh}^H & d_{gh}^V & d_{gh}^D \\ d_{hg}^H & d_{hg}^V & d_{hg}^D \\ d_{gg}^H & d_{gg}^V & d_{gg}^D \end{bmatrix} \\ &= \begin{bmatrix} \psi_h(x)\phi_h(y) & \phi_h(x)\psi_h(y) & \psi_h(x)\psi_h(y) \\ \psi_g(x)\phi_h(y) & \phi_g(x)\psi_h(y) & \psi_g(x)\psi_h(y) \\ \psi_h(x)\phi_g(y) & \phi_h(x)\psi_g(y) & \psi_h(x)\psi_g(y) \\ \psi_g(y)\phi_g(y) & \phi_g(y)\psi_g(y) & \psi_g(y)\psi_g(y) \end{bmatrix} \end{aligned}$$

495 Columns of the above matrix correspond to quaternion wavelet functions of
 496 the horizontal sub-band d^H , the vertical sub-band d^V , and diagonal sub-band
 497 d^D from left-to-right respectively. The three according wavelet coefficients are
 498 d_s^H , d_s^V and d_s^D and the $\stackrel{q}{=}$ operator means formation of quaternion number
 499 by coefficients along each column. Though quaternion wavelet coefficients
 500 possess rich phase information, our research currently focuses on magnitudes
 501 of each wavelet sub-bands. Therefore, magnitudes of horizontal, vertical
 502 sub-bands can be computed according to quaternion magnitude formula as
 503 follows.

$$\begin{aligned} \|d_s^H\| &= \sqrt{(d_{hh}^H)^2 + (d_{gh}^H)^2 + (d_{hg}^H)^2 + (d_{gg}^H)^2} \\ \|d_s^V\| &= \sqrt{(d_{hh}^V)^2 + (d_{gh}^V)^2 + (d_{hg}^V)^2 + (d_{gg}^V)^2} \\ \|d_s^D\| &= \sqrt{(d_{hh}^D)^2 + (d_{gh}^D)^2 + (d_{hg}^D)^2 + (d_{gg}^D)^2} \end{aligned}$$

504 While the final approximated version of input signals, which are not decom-
 505 posed further by the transform, have its magnitude computed by quaternion

506 algebra.

$$\begin{aligned} \|c_S\| &= \sqrt{(c_{hh})^2 + (c_{gh})^2 + (c_{hg})^2 + (c_{gg})^2} \\ &= \sqrt{(\phi_h(x)\phi_h(y))^2 + (\phi_g(x)\phi_h(y))^2 + (\phi_h(x)\phi_g(y))^2 + (\phi_g(y)\phi_g(y))^2} \end{aligned}$$

507 *5.4. Quaternion Wavelet Packet Transform*

508 To construct a packet form of QWT, each and every sub-band c_S, d^H, d^V, d^D
509 should be repeatedly decomposed by low-pass (h_0, g_0) and high-pass filters
510 (h_1, g_1) . Bayram *et al*[32] has investigated into formation of wavelet pack-
511 ets for DT-CWT, an equivalent form of QWT. In order to get an analytic
512 quaternion wavelet packet, the filter banks need to be chosen in a specific
513 way such that the Hilbert transform relationship is preserved. In Bayram's
514 works [32], the analytic wavelet transformed can be achieved if whatever
515 filter-bank is used to decompose the first filter-bank of QWT should also be
516 used for the second (dual) filter-banks. Another important point about the
517 extension to wavelet packet QWPT is the choice of the extension filters $f_i(x)$.
518 It has been found that the only necessary constrain to preserve the Hilbert
519 transform property is forcing the usage of the same filter-pairs $f_0(x), f_1(x)$ in
520 both filter-banks of QWT or DT-CWT. Therefore, any CQF pair of filter-
521 banks with short support, frequency selectivity or possessing a number of
522 vanish moments can be candidates for the extension filter. Noted that, the
523 above criteria such as CQF pair of filters have been employed for extending
524 a regular DWT. Like other derivatives of DT-CWT or QWT, the quater-
525 nion wavelet packet transform (QWPT) are approximately shift-invariant,
526 which means the energy in each sub-band is approximately preserved if the
527 input signals are shifted by a number of samples. Noteworthy that, there are
528 other methods beside QWPT with shift-invariant property in wavelet pack
529 decomposition. For example, by performing an exhaustive search over all
530 shifted wavelet packet bases to find the "best basis" according to a certain
531 cost function [33], the orthonormal wavelet packet transform becomes shift-
532 invariant in a sense that energy in each sub-band is invariant to transition of
533 input signals. This (approximately) shift-invariance property becomes very
534 useful and important in the search for a suitable energy descriptors. This
535 shift-invariance property guarantees that DT-CWT, DT-CWPT or QWT,
536 QWPT would have energy descriptors robust to certain amount of affine
537 transformation in input signals.

538 Interactions of filtering both low and high components at each stage of
539 DT-CWT introduces a complete structures of all possible sub-bands that

540 can be generated by the filter-bank pair. Each tree forms a unique frequency
541 profile of input signals. Among those countless numbers of possibilities, there
542 exist a frequency decomposition being more sparse and compact than the
543 others. It is called the best-basis in terms of representing the input signals
544 with fewest wavelet coefficients. A fast algorithm for indicating such best
545 basis has been reported in extension from DWT to DWPT [28]. In addition,
546 it is previously mentioned in the section 5.2, the same strategy can be adopted
547 for searching best-basis in QWT. In brief, the approach is looking for a path
548 in a binary of decomposition to minimize a Shannon entropy cost function;
549 more details can be found in the work of Coifman *et al*[28]. After “best
550 basis” searching for QWPT decomposition, we can identify magnitudes and
551 energy of coefficients at a specific location by a simple quaternion algebra.
552 $\|q(a, b, c, d)\| = \sqrt{a^2 + b^2 + c^2 + d^2}$.

553 6. Wavelet Coefficients Correlation

554 The previous section 4 have discussed the potential of using energy den-
555 sity distribution of localized time-scale element or wavelet elements instead
556 of pixel-value probability distribution. Only general 1-D signal is considered
557 and these elements are assumed to be independent or at least linearly in-
558 dependent (uncorrelated); however, this assumption only works for random
559 variables as input signals. Practically, except total noise, any meaningful sig-
560 nals often has specific structures persistent across multiple time-scale element
561 in 1-D case. For 2-D signals like natural images, an additional orientation
562 needs considering; in other words, their wavelet coefficients are highly sta-
563 tistically related across scales, orientation, spaces. This phenomenon is sys-
564 tematically studied and confirmed in Azimifar *et al*research [34]. The author
565 has conducted an empirical study of joint wavelet statistics for texture and
566 natural images to investigate correlation relationship between neighbouring
567 coefficients. Examination of these dependencies helps propose appropriate
568 models for such a transform-domain algorithm. Though Azimifar’s work [34]
569 only covers linear dependencies and just a squint on non-linear relations, its
570 proposals are evaluated on a collection of 5000 real images. Therefore, we
571 believe her conclusion in that study is generally true at least for natural im-
572 ages, the main researching objects. In brief, there exists a few elementary
573 correlation relationships as follows.

- 574 • The spatially-localized and sparse correlation structure has a clear per-
575 sistence across scales.

- 576 • Every coefficient exhibits correlations extending across multiple scales,
577 with spatially near neighbors both within and across orientations.
- 578 • A subband coefficients at the same spatial locations but from different
579 orientations are not linearly correlated.
- 580 • Within-subband, inter-subband, and inter-scale correlations are highly
581 oriented and persistent across local neighbors of its parent.

582 The below figure 4 clearly illustrates all mentioned correlations, their prefer-
583 ences to locality as must be expected. This locality increases toward finer
584 scales, which supports persistency property of wavelet coefficients. A single
585 coefficient correlates with its parents as well as neighbors across orientations
and scales. Among several mentioned statistical dependencies, the most vi-

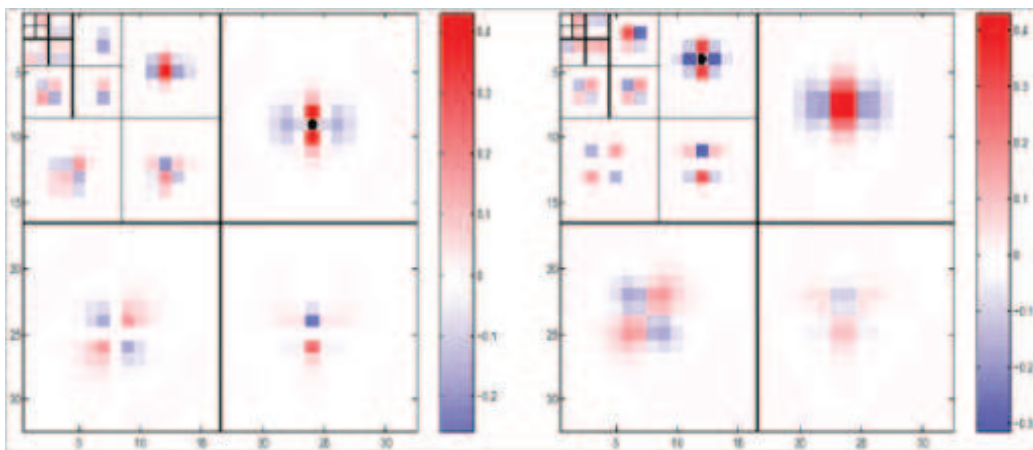


Figure 4: Illustration of wavelet coefficients inter-band and intra-band correlation [34]

586 tal findings for our work are uncorrelated siblings coefficients across orien-
587 tation and strong correlated coefficients across scales since it theoretically
588 allows uncertainty and mutual information estimation of a 2D time-scale
589 element or a wavelet sub-band energy descriptor. To elaborate this point,
590 lets consider two adjacent scales s_1, s_2 and their corresponding coefficients
591 $w_i f(x, y, s_1)$ of horizontal, vertical, diagonal orientation $i = v, h, d$ for 2-D
592 signals $f(x, y)$. Due to non-correlation of sibling coefficients across orien-
593 tation, it is possible to consider three wavelet coefficients as a multivariate
594 variable $W_s = (w_h, w_d, w_v)$ with uncertainty estimation by energy density
595 distribution across three orientations $H(W_s)$. For two adjacent sub-band
596

597 s_1, s_2 , there are two multivariate variables W_{s_1} and W_{s_2} corresponding two
 598 entropy values $H(W_{s_1})$ and $H(W_{s_2})$, and the mutual information between
 599 two variables due to inter-scale dependencies between correspondent wavelet
 600 coefficients are computed as follows.

$$I(W_{s_1}, W_{s_2}) = H(W_{s_1}, W_{s_2}) - H(W_{s_1}) - H(W_{s_2}) \quad (6)$$

601 From that basic observation about inter-scale and intra-scale wavelet coef-
 602 ficients of natural images is developed the core idea of our proposal. More
 603 details about sub-band energy descriptors and how to measure their uncer-
 604 tainty and mutual information will be clearly explained in following sections
 605 6.1, 6.2

606 6.1. Interscale Subband Energy Descriptor

607 Interesting relationship between basis-project methods and scale saliency
 608 are repeatedly discussed in several publications[7], [13]. Kadir [7] actually dis-
 609 cusses about behaviours of non-saliency and saliency regions in spectral and
 610 wavelet domain. A simple, flat, non-salient regions or images is sufficiently
 611 described by a single sub-band; meanwhile, complicated data and structure
 612 regions require more sub-bands descriptors. This directly introduces basis-
 613 projected sub-bands as potential alternative descriptors. Like pixel-value
 614 descriptors, real wavelet sub-bands must be treated as discrete variables due
 615 to its theoretical restriction, data-analysis uncertainties, $\sigma_t \sigma_\omega \geq \frac{1}{2}$. In other
 616 words, it is impossible for continuous wavelet sub-bands distribution at any
 617 specific location. Following available mathematical definition of PSS for dis-
 618 crete pixel descriptors, we sketch rough mathematical models of WSS with
 619 discrete sub-band descriptors, $\{e \in \mathbf{E}, \mathbf{E} = \{e_1, e_2, \dots, e_m\}\}$, in the equations
 620 7, 8, 9, 10 whereof e, E are a element and set of sub-band descriptor consec-
 621 utively.

$$Y_D(\vec{s}_p, \vec{x}) \triangleq H_D(\vec{s}_p, \vec{x}) W_D(\vec{s}_p, \vec{x}) \quad (7)$$

$$H_D(s, \vec{x}) \triangleq - \sum_{d \in D} p_{b,s,\vec{x}} \log_2 p(d, s, \vec{x}) \quad (8)$$

$$W_D(s, \vec{x}) \triangleq \frac{s^2}{2s-1} \sum_{d \in D} |p_{b,s,\vec{x}} - p_{b,s-1,\vec{x}}| \quad (9)$$

$$\vec{s}_p \triangleq \{s : H_D(s-1, \vec{x}) < H_D(s, \vec{x}) > H_D(s+1, \vec{x})\} \quad (10)$$

However, a general concept of sub-band descriptor is not useful in actual com-
 putation; therefore, an appropriate numerical attribute of sub-bands need

proposing instead. Lets consider 2-D discrete real-wavelet transform with three sub-bands vertical (v), horizontal (h) and diagonal (d) sub-bands at each particular dyadic scale s represented by three set of wavelet coefficients (\mathbf{w}_i) accordingly in the equation 11. Equation 12 uses those coefficients to compute sub-band energy densities as descriptors (e) for Wavelet-domain Scale Saliency (WSS).

$$\mathbf{w}_i f(x, y, s_j)|_{i=\{v,h,d\},s_j=\{s_1,s_2,\dots,s_n\}} = f(x, y) * \psi_{s,i}(x, y, s_j) \quad (11)$$

$$\mathbf{P}\{\mathbf{w}_i f(x, y, s_j)\}|_{i=\{v,h,d\},s_j=\{s_1,s_2,\dots,s_n\}} = |\mathbf{w}_i f(x, y, s_j)|^2 \quad (12)$$

622 In the standard real discrete wavelet transform (DWT), there are fixed three
 623 analysed sub-bands for each dyadic sampling step. Supposedly the maximum
 624 level of wavelet decomposition is n , the number of dyadic scales is n with 3
 625 sub-bands for each scale. With 4 or 5 as the usual number of decomposition
 626 levels, totally around 12 or 15 sub-bands descriptors are analysed for an
 627 image. This number of descriptors is significantly less than 255 pixel-value
 628 descriptors of PSS for any grey-scale image.

Besides wavelet transforms, different other types of basis projection techniques could also be utilized; for example, best basis wavelet packet analysis (DWPTBB). The full wavelet packet transform breaks signals into sub-bands with the same bandwidth at the maximum dyadic scale. It would not fit into the scale saliency concept which requires descriptors at different scales. Fortunately, the "balanced" full wavelet packet tree usually over-describes image properties, and the description can be optimized by Best Basis (B^2) finding operation. The optimized wavelet packet tree often has projected basis across dyadic scales since some small image details are best described with a basis at finer resolution while other big details prefer another basis with coarser resolution. The DWPTBB coefficients are utilized for sub-band energy density, the proposed image descriptors, calculation in the equations 13, 14.

$$\mathbf{w}_i f(x, y, s_j)|_{(i,j)=B^2(\mathbf{w}_i f(x,y,s_j))} = f(x, y) * \psi_{s,i}(x, y, s_j) \quad (13)$$

$$\mathbf{P}\{\mathbf{w}_i f(x, y, s_j)\}|_{(i,j)=B^2(\mathbf{w}_i f(x,y,s_j))} = |\mathbf{w}_i f(x, y, s_j)|^2 \quad (14)$$

629 Comparing mathematical statements 11,12 and 13,14 for sub-bands descrip-
 630 tors of Discrete Wavelet Transform (DWT) and Discrete Wavelet Packet
 631 Transform Best Basis (DWPTBB) consecutively, we can see their fundamen-
 632 tal differences. While DWT provides determinant basis-projection methods
 633 with pre-computed basis and fixed structure of sub-bands, DWPTBB adapts

634 itself into each data set. Then, its number and structure of sub-bands are
 635 specified by Best Basis (B^2) finding operator [28]. It requires more opera-
 636 tions; however, more faithful and adaptive descriptors can be achieved.

Both DWTBB and DWT are popular wavelet-transforms; however, they both depend on shift-variant real discrete wavelet transforms. It means that projection of coefficients not only depends on data but also its relative location on the scene.

$$\mathbf{w}_i f(x, y, s_j) \neq \mathbf{w}_i f(x + \Delta(x), y + \Delta(y), s_j) \quad , \exists x, y, s_j, \mathbf{w}_i, \Delta(x), \Delta(y) \quad (15)$$

$$P\{\mathbf{w}_i f(x, y, s_j)\} \neq P\{\mathbf{w}_i f(x + \Delta(x), y + \Delta(y), s_j)\}, \exists x, y, s_j, \mathbf{w}_i, \Delta(x), \Delta(y) \quad (16)$$

As the fourth criteria for good information measurement of Starck *et al*[17] states that entropy must work in the same way regardless of descriptors' locations. Both DWT and DWTBB projected descriptors do not satisfy that condition since usages of these descriptors might lead to different information estimation for identical data at two different locations. The shift-variance of real-wavelet transform can be avoided by complex wavelet transform design; for instances, recently developed dual-tree complex wavelet transform (DTCWT) [35], Quaternion wavelet transform (QWT) [26], or dual-tree complex wavelet packet transform with best-basis (DTCWTBB) [32]. General formula of complex coefficients and their corresponding sub-band energy density are summarized in the equations 17,18.

$$\mathbf{w}_i f(x, y, s_j)|_{i=\{\{v,h,d\} \vee B^2(\mathbf{w}_i f)\}} = f(x, y) * (\psi_{g,s,i}(x, y, s_j) + j\psi_{h,s,i}(x, y, s_j)) \quad (17)$$

$$\mathbf{P}\{\mathbf{w}_i f(x, y, s_j)\}|_{s_j=\{s_1, \dots, s_n\} \vee B^2(\mathbf{w}_i f)} = \|\mathbf{w}_i f(x, y, s_j)\|_2^2 \quad (18)$$

637 Dual-tree approaches use two different wavelet filter-banks, $\{\psi_g, \psi_h\}$, and
 638 they are designed to form analytical complex filter banks, $\{\psi_g(x, y) + j\psi_h(x, y), \psi_h(x, y) \approx$
 639 $H(\psi_g(x, y))\}$. The magnitudes of projected-complex coefficients are proven
 640 to be shift-invariant; therefore, its derived energy density of the sub-bands
 641 is as well shift-invariant. Probably, the quaternion version of wavelet trans-
 642 form (QWT) and quaternion wavelet packet transform best basis (QWTBB)
 643 with shift-invariant property would provide better descriptors than their real
 644 counterparts according to five criteria of Starck [17].

645 *6.2. Intra-scale Subband Energy Descriptor*

646 As previously mentioned in the section 6, there is strong correlation or
 647 statistic linear dependence between wavelet coefficients in natural images.
 648 The first correlation, the inter-scale dependencies, has been discussed in the
 649 section 4,6, and modeled as sub-band descriptors in the previous section 6.1.
 650 Moreover, the relation have been widely and effectively employed in various
 651 tree-structured coding techniques such as SPIHT [36]. Besides inter-scale
 652 relationship, many authors [25] have pointed out another strong correlation of
 653 intra-band coefficients existing across many different types of natural scenes
 654 . Minh Do and M Vetterli [25] successfully modelled coefficients of a wavelet
 655 sub-band with a simple explicit mathematical form, Generalized Gaussian
 656 Distribution (GGD). While statistical distribution of wavelet coefficients gets
 657 a lot of interest, several researches have proposed different mathematical
 658 models for analysing this statistical characteristic. However, few models of
 659 wavelet coefficients marginal density at a particular sub-band works better
 660 than GGD in terms of accuracy, approximation and simplicity. After such
 661 the distribution is widely observed in experimental data with natural images,
 662 theoretical analysis on the plausibility of modelling by the GGD distribution
 663 is defined as follows.

$$p(x; \alpha, \beta) = \frac{\beta}{2\alpha\Gamma(1/\beta)} e^{(-|x|/\alpha)^\beta}$$

664 where $\Gamma(z) = \int_0^\infty e^{-t} t^{z-1} dt$, $z > 0$ is the Gamma distribution. Here α dic-
 665 tates the scale parameter or variance of the distribution, and β controls
 666 shapes. For example, GGD with $\beta = 1$ is Gaussian distribution; it becomes
 667 Laplacian distribution with $\beta = 2$.

668 **7. Information Measurement**

669 In the previous section 6.1, four different wavelet transforms generate cor-
 670 responding wavelet sub-band energy density descriptors. From those energy
 671 density, energy probability distribution function (*PDF*) at each scale s_j can
 672 be computed as follows.

$$\begin{aligned} p_{interband}(x, y, s_j) &= p\{\mathbf{P}[\mathbf{w}_i f(x, y, s_j)]\}_{i=\{v,h,d\} \vee i=B^2(\mathbf{w}_i)}, j <= m \\ &= \frac{\mathbf{P}[\mathbf{w}_i f(x, y, s_j)]}{\sum_j \sum_i \mathbf{P}[\mathbf{w}_i, f(x, y, s_j)]} \end{aligned}$$

673 The above formula computes the probability of energy density at one loca-
674 tion (x, y) across different sub-bands, $i = \{v, h, d\}$ for (DWT) or (QWT)
675 or $i = B^2(\mathbf{w}_i)$, for (DWPTBB) and (QWPTBB) from the smallest scale, 1,
676 to currently considered scales, m . The first level uses the smallest sampling
677 window size of wavelet atoms; therefore, it generates analysed coefficients
678 with finest details. Then, the sampling window sizes are doubled after each
679 level; they generate coarser analysed details. It is quite similar to PSS sam-
680 pling operations except that scales are doubled rather than increased by a
681 unit. Like *PDF* of PSS descriptor, WSS descriptors *PDF* are distributed
682 with increasing scales of j , from level 1 (smallest wavelet atom) to level m
683 (currently biggest wavelet atom). From the equation 19, it is straightfor-
684 ward to compute feature-space entropy $H_{Observer}(x, y, s_m)$ as follows whereof
685 $p\{\mathbf{P}[\mathbf{w}_i f(x, y, s_j)]\}$ is shorted as $p_{interband}(x, y, s_j)$.

$$- \sum_{\{i=\{v,h,d\} \vee i=B^2(\mathbf{w}_i)\}, \{j \leq m\}} p_{interband}(x, y, s_j) \log p_{interband}(x, y, s_j) \quad (19)$$

686 Both entropy of PSS's descriptors and the above entropy formula for the
687 proposed descriptor only summarizes statistical property in local spatial re-
688 gions since both considering window sizes in PSS and scale levels of wavelet
689 decomposition are finite. Then, it lacks involvement of energy distribution in
690 the whole image and it is confirmed that such distribution is vital for natural
691 image and texture modeling [25]. As presented in the sub-section 6.2 is the
692 Generalized Gaussian Distribution of coefficients magnitudes from a wavelet
693 intra-band.

$$p_{intra-band}(x, y, s_j, \alpha, \beta) = \frac{\beta}{2\alpha\Gamma(1/\beta)} e^{(-\sqrt{x^2+y^2}/\alpha)^\beta} \quad (20)$$

694 In order to combine both global and local characteristics into a single
695 value, we propose cross-entropy $H_{Searcher}(x, y, s_m)$ between inter-band and
696 intra-band distribution as an alternative formulation of the equation 19.

$$- \sum_{\{i=\{v,h,d\} \vee i=B^2(\mathbf{w}_i)\}, \{j \leq m\}} p_{interband}(x, y, s_j) \log p_{intra-band}(x, y, s_j) \quad (21)$$

697 To distinguish between two modes of entropy computation, we names
698 the local entropy by the equation 19 as "observer" mode, and the cross-
699 entropy involving both local and global statistics as "searcher" mode. In later

700 formula, when general entropy symbol H without specific subscripts appears
 701 in any formulas, it means both modes are eligible for those equations. Those
 702 names also help to distinguish different parameters and simulation modes
 703 presented in the experimental sections 8.2.

704 The equation 19 computes feature-space entropy of sub-band energy de-
 705 scriptors for WSS as the equation 8 does for PSS. Half of scale saliency
 706 measure, feature-space entropy, has been figured out for sub-band energy
 707 density descriptors. The other half of the problem rests in computational
 708 details of inter-scale saliency; in other words, how the equation 9 should
 709 be interpreted with the proposed descriptors. In equation 8, the inter-scale
 710 saliency is measured as total variation in probability distribution of descrip-
 711 tors at two consecutive scales in which pixel-value descriptors (d) appear
 712 in both distributions, it complicates the problem. However, the situation
 713 is different for wavelet sub-band energy density descriptors since each sub-
 714 band in the current level is unique for this level only. It does not appear
 715 in other levels of analysis. This wonderful property simplifies out task in
 716 building sub-band probability distribution for different levels but makes the
 717 equation 3 inappropriate for sub-band features. Since it is unjustifiable to
 718 find total variation of two PDF on two different set of descriptors, an alter-
 719 native interpretation of inter-scale saliency need developing. Lets consider
 720 $P(M) = \{p_{i,j}(x, y, s_j) | \forall i, j \leq m\}$, PDF of all sub-bands up to the current
 721 level, m . When a new analysed sub-band, $D = \{p_{i,j}(x, y, s_j) | j = m + 1\}$,
 722 is generated, this sub-band descriptor will modify the current PDF into
 723 $P(M|D)$. The distance between the prior model and the modified model can
 724 be measured by Kullback-Leibler divergence as follows.

$$K(P(M|D), P(M)) = \int_M P(M|D) \log \frac{P(M|D)}{P(M)} \quad (22)$$

725 Noteworthy, it is similar to Itti's Bayesian Surprise Saliency (BSS) metric
 726 [14], and the surprise model can be extended for multiple sub-bands de-
 727 scriptors or evidences in BSS. The equation 22 becomes mutual information
 728 between the current model and a set of new evidences. In other words, the
 729 expectation of surprise for adding new sub-bands into the current model
 730 is the mutual information between new sub-bands and the current model,
 731 shown in the equation 23.

$$MI(D, M) = \int_D K(P(M|D), P(M)) = \int_{D,M} P(D, M) \log \frac{P(D, M)}{P(M)P(D)} \quad (23)$$

Therefore, mutual information is chosen as inter-scale saliency for successive dyadic scales since it actually implies averaged "bayesian surprise" [14] saliency of sub-bands across scales. Furthermore, mutual information as inter-scale saliency measurement well emphasizes the structural coherence of data across scales. If there are useful structures such as edges or joints and they are consistent across consecutive scales, they will increase mutual information between two consecutive scales. Otherwise noises have no mutual information across scales as its self-information is zero, $I(N, N) = 0$. It is remarkable that mutual information satisfies the fifth criterion of the good information estimation by Starck *et al*[17]. The only remaining step is identifying how the mutual should be calculated in discrete cases. Following formula shows relation between mutual information and entropy.

$$MI(D, M) = H(D) + H(M) - H(D, M) \quad (24)$$

$$H(M) = - \sum_{\{i=\{v,h,d\} \vee i=B^2(\mathbf{w}_i), \{j \leq m\}\}} p_i(x, y, s_j) \log p_i(x, y, s_j) \quad (25)$$

$$H(D) = - \sum_{\{i=\{v,h,d\} \vee i=B^2(\mathbf{w}_i), \{j=m\}\}} p_i(x, y, s_j) \log p_i(x, y, s_j) \quad (26)$$

$$H(D, M) = - \sum_{\{i=\{v,h,d\} \vee i=B^2(\mathbf{w}_i), \{j \leq m+1\}\}} p_i(x, y, s_j) \log p_i(x, y, s_j) \quad (27)$$

The mutual information can be directly calculated as difference between separated ($H(D) + H(M)$) and joint ($H(D, M)$) entropy estimation of the current energy descriptors (the current model) and the next-level sub-bands, the equation 24. While the entropy elements $H(D)$, $H(M)$, $H(D, M)$ can be easily estimated by simple mathematical equations 25,26,27. The joint entropy $H(D, M)$ can be reused as $H(M)$ for the next level inter-scale saliency estimation because of the sub-band descriptors uniqueness. The scale saliency principles on wavelet-domain sub-band energy descriptors are summarized in the equation 28 as product of maximum feature-space saliency and inter-scale saliency, or product of mutual information between consecutive levels and maximum sub-band entropy.

$$H(M(x, y, s_p)) = - \sum_{i=\{v,h,d\} \vee i=B^2(\mathbf{w}_i), j \leq m} p_i(x, y, s_p) \log p_i(x, y, s_p)$$

$$MI(D(x, y, s_p), M(x, y, s_p - 1)) = H(D) + H(M) - H(D, M)$$

$$\vec{s}_p \triangleq \{s : H(M(s - 1, x, y)) < H(M(s, x, y)) \wedge H(M(s, x, y)) > H(M(s + 1, x, y))\}$$

$$Y(M(x, y, s_p)) = H(M(x, y, s_p)) * MI(D(x, y, s), M(x, y, s_p - 1)) \quad (28)$$

The characteristic scale s_p is chosen to maximize information of the model $H(M(s, x, y))$. Lets imagine the case prior scale contains only noise meanwhile later scales actually contain useful structures of images. With bias of Shannon entropy toward noise, the characteristic scale fails to enclose any useful structure. To overcome this drawback, we propose alternative approach, **DIS** to differentiate from the original strategy *WSS*, in which s_p is selected so as to maximize inter-scale saliency or average "Bayesian surprise". **DIS** principles can be summarized as follows.

$$\vec{s}_p \triangleq \{s : MI(D_{s-1}, M_{s-2}) < MI(D_s, M_{s-1}) \wedge MI(D_s, M_{s-1}) > MI(D_{s+1}, M_s)\}$$

732 Experiments with **DIS** and **WSS** are carried out and simulations results are
 733 detailed in the next section in order to confirm effectiveness of the proposed
 734 strategy.

735 8. Discussion & Results

736 The previous sections 6.1 and 7 have analysed theoretical advantages of
 737 **WSS** and its derivative **DIS**. In addition, the subsection 6.1 present four
 738 descriptors based on different wavelet transforms: DWT, QWT, DWPTBB,
 739 and QWPTBB. Accordingly, we have several derivatives for the proposed
 740 method according to specific choices of scale section mechanisms and sub-
 741 band descriptor. To evaluate them against other saliency approaches, they
 742 are compared with PSS [7], and the de-facto ITT model [3]. The purpose of
 743 comparisons are not for claiming the best saliency method or racing toward
 744 the highest possible evaluating measurement; it just proves the rationale of
 745 the assumption that feature and structural complexity would be a good clues
 746 for human attention. The best evaluation measurement reported does not
 747 necessarily mean the best saliency maps since it much depends on choices
 748 of databases, elimination of experimental bias, performance of human test
 749 subjects, etc. Moreover, a standardized evaluation process in saliency map
 750 evaluation is far from being reached since several researchers choose differ-
 751 ent database and measurement methods or even create their own. In our
 752 research, we focus on the effectiveness of information measurement in visual
 753 attention; then, the most common processes and databases would be chosen
 754 to confirm generalization of the assumption.

755 In line of searches for informative clues , Bruce and Tsotsos [15] database
 756 is certainly among the popularly used stimuli. However, only Bruce's database

757 is certainly not enough due to limits in numbers and contents of stimuli.
758 Then, Kootstra’s database [16] are chosen for extra testing samples and
759 ground-truths. Two database with over 200 samples with ground-truths
760 provided by more than 50 human subjects would help to confirm the gen-
761 eralization of our proposed framework to a certain extent. Similarly, only
762 common evaluation approaches are deployed in our studies, and they can
763 be categorized into either quantitative or qualitative methods. Quantitative
764 relations between different saliency methods and human visual performance
765 are shown by appropriate statistical methods (AUC,NSS) with eye-tracking
766 data as ground-truths. Meanwhile, the qualitative results, visual compar-
767 isons of different saliency maps, gives a glimpse about performance for each
768 individual sample. It also specifies imaging contexts where saliency meth-
769 ods give reasonable solution as well as situations where saliency maps are
770 unreasonable to human perception.

771 *8.1. Databases of image stimuli*

772 The ground-truth and data for basic evaluations of visual saliency per-
773 formance is got from eye-tracking experiments. Specially in Neil Bruce
774 database, 120 different color images are observed in random orders while
775 there are 4 seconds gap between the previous and the next stimuli. To en-
776 sure consistency and accuracy of the database, subjects are asked to seat
777 0.75 m in front of a 21 inch CRT monitor. Especially, human subjects have
778 no further instructions for any actions or clues for what images appear next.
779 Furthermore, image contents are varied from indoor to outdoor environments.
780 Sometimes, there are clear interesting objects in the scene; while some scenes
781 are really general without any particular interests in any subjects. A non-
782 head mount eye tracking apparatus extracts locations of eye-fixation while
783 human test subjects look at sample images. Other setting-up parameters
784 are intended for a general-scene based stimuli which are typically found in
785 urban environments. Moreover, the same parameters are used for collect-
786 ing data from 20 different subject over 120 testing samples. The following
787 figure 5 shows first eight images from the Neil Bruce’s database. Despite
788 its popularity, images from Neil Bruce’s database has narrow semantic con-
789 tent since it contains only urban scenes and mainly indoor environments.
790 Besides that, the number of samples are relatively small. Due to that, an
791 additional database should be included in simulations such that there more
792 testing images of natural objects like animals, flowers, in natural environ-
793 ments. Kootstra’s database [16] have just satisfied these requirements with



Figure 5: Neil Bruce's database

794 additional ground-truths for further experiments. Kootstra's ground-truths
 795 data are also collected from eye-tracking experiments although the exper-
 796 imental process is slightly different from what have been done to collect
 797 Bruce's database. In the psychological experiment, with head-mount eye-
 798 tracking devices, thirty-one students (15 men, 16 womens) ranging from 17
 799 to 32 of age took part in the experiments, and they are all naive about aims
 800 of experiments. Each human subject observes a total of 99 photographic
 801 image in five different categories while their eye movements are recorded si-
 802 multaneously with the head-mounted device. There are nine-teen images in
 803 natural symmetry category; each of which contains symmetrical natural ob-
 804 jects. Beside such symmetrical scenes, other non-symmetrical photographic
 805 scenes are included into the image sets such as: 12 images of animals in nat-
 806 ural seeting, 12 images of street environments, 12 images of street scenes, 16
 807 images of building and 40 images of natural environments. Figure 6 gives an
 808 example of 5 categories of images in the Kootstra's database. Noted that,
 809 each image is presented to viewers with a resolution of 1024x768 pixels on
 810 an 18" CRT monitor at a distance of 70 cm from the participant.

811 *8.2. Quantitative Comparisons of Saliency Methods*

812 The quantitative performance includes Receiver Operating Characteris-
 813 tics (ROC) curves with Area Under ROC Curve (AUC), and Normalized
 814 Scanpath Saliency (NSS) as numerical results. To ensure fair comparisons
 815 between methods, open-source evaluation codes for AUC and NSS [37] are
 816 employed. Noteworthy, saliency maps are standardized around median in-
 817 stead mean of distributions. Quantitative evaluation of visual saliency map



Figure 6: Kootstra's database

818 on natural images with eye-tracking data ground has been initially studied by
 819 Tatler and recently summarized by Borji *et al*[37]. More information about
 820 mechanisms behind ROC and AUC can be found [37]. In this section, we
 821 only focus on usages of these quantitative methods to compare, evaluate and
 822 prove rationale of our approach. As the main purpose of this evaluation is
 823 confirming effectiveness of informative clues in human's visual attention, our
 824 approach is not optimally tuned to reach the maximum AUC or NSS.

825 All four descriptors mentioned in the section 6.1 have been simulated with
 826 image samples from both Neil Bruce's and Kootstra's datasets. Noted that
 827 scale selection mechanisms have strong influences in formation of saliency
 828 maps; therefore, two separated simulations are carried out to investigate
 829 that effect as well. Figure 7 and 8 summarizes simulations results of proposed
 830 methods with corresponding WSS and DIS respectively in Neil Bruce's image
 831 dataset.

832 According to the figure 7 and the table 2, performances of four WSS
 833 derivatives follow decreasing orders: DWT, QWT, DWPTBB and QW-
 834 PTBB; however, all are better than PSS performance and comparable to ITT
 835 method. Especially, a computational time is deducted by approximately 7
 836 times; noteworthy, the PSS is implemented in C++ with MATLAB interface
 837 and WSSs are totally written in MATLAB. For Niel Bruce database, the best

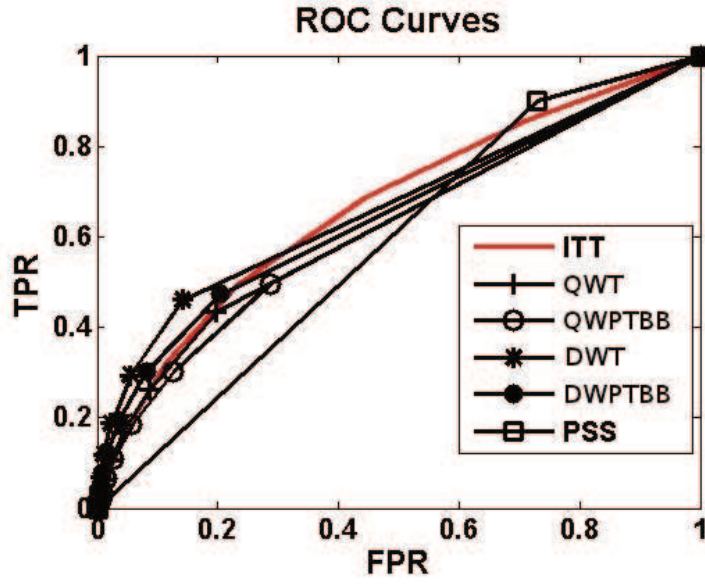


Figure 7: ROC Curve - WSS

MTH	AUC	NSS	TIME(s)
ITT	0.6944	0.27714	1.096s
PSS	0.5856	-0.39175	7.1092s
DWT	0.67823	0.33358	1.2401s
QWT	0.66279	0.30002	1.9231s
DWPTBB	0.6417	0.26079	2.6187s
QWPTBB	0.63529	0.23714	5.2836s

Table 2: Quantitative Result

838 basis approaches *DWPTBB* and *QWPTBB* does produce poorer results in
 839 both accuracy test, AUC and NSS as well as efficiency test, TIME.

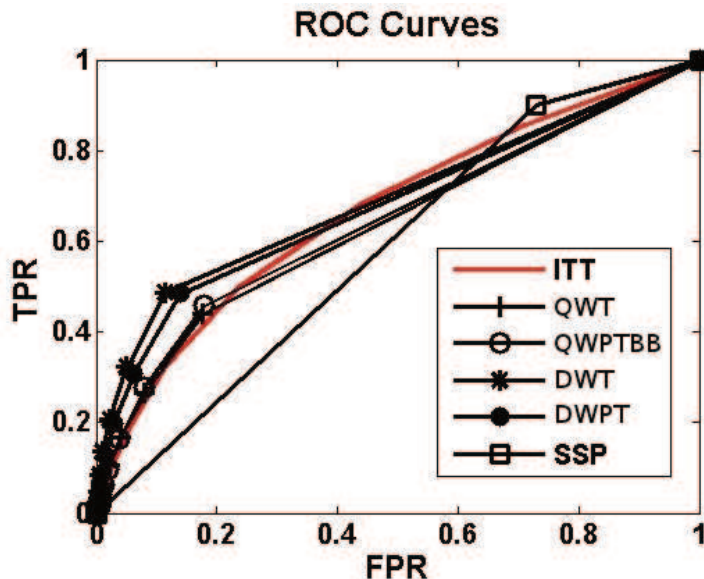


Figure 8: ROC Curve - DIS

MTH	AUC	NSS	TIME(s)
ITT	0.6944	0.27714	1.096s
PSS	0.5856	-0.39175	7.1092s
DWT	0.7028	0.3178	1.2689s
QWT	0.6922	0.3024	1.9527s
DWPTBB	0.6299	0.2546	2.4218s
QWPTBB	0.6394	0.2351	5.4835s

Table 3: Quantitative Result

840 Quantitative performances of four **DIS** methods are shown in the fig-
 841 ure 8 and the table 3. Mixed results are spotted. Performances of DWT
 842 and QWT descriptors with DSS approach are a little bit increased in terms
 843 of AUC if compared to the case of WSS. However, "Best-basis" descriptors
 844 (DWPTBB, QWPTBB) perform a little bit better if WSS are employed in-
 845 stead of DIS. Meanwhile, there is almost no difference between WSSs and
 846 DSSs in term of both NSS and TIME regardless descriptors.

847 Above is shown simulation results from Neil Bruce image data-set with
 848 eye-tracking locations. Despite of its recently popular database in evaluating
 849 saliency maps, the data-set has limitations analysed in the subsection 8.1.
 850 Another sets of images should be brought in to enhance diversity of testing
 851 samples. Kootstra’s database with more image categories and all eye-tracking
 852 data ground truth is a perfect candidate. Additional simulation results would
 853 confirm and generalize rationale of our proposed information-based saliency
 854 methods. Similar to the table 2, figure 7, the table 4 and figure 9 demonstrate
 855 how well the proposed methods with four descriptors and WSS scale selection
 856 mechanism perform against other saliency methods like ITT and PSS.

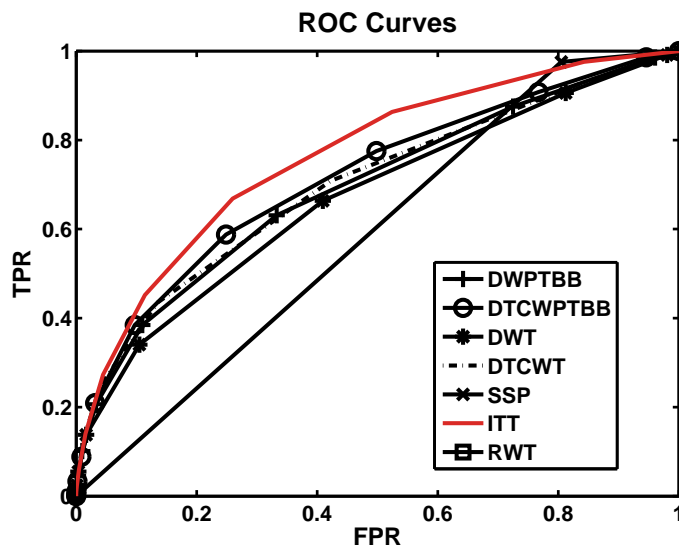


Figure 9: ROC Curve - WSS

MTH	AUC	NSS	TIME(s)
ITT	0.7819	0.5144	2.3874
PSS	0.5852	-0.3532	17.0663
DWT	.7150	0.4849	.4414
QWT	.7301	0.5070	2.9313
DWPTBB	0.7242	0.4631	4.9577
QWPTBB	0.7612	0.3922	4.7743

Table 4: Quantitative Result

857 Among four descriptors, the best result in terms of AUC is from QW-
 858 PTBB descriptor, and the second best is QWT; while both DWT and DW-
 859 PTBB have nearly equal AUC values. Comparing with ITT and PSS, QW-
 860 PTBB's performance in AUC measurement is nearly equal to that of ITT
 861 and much larger than PSS. The result strengthens our hypothesis about
 862 usefulness of informative clues in saliency map construction. Moreover, it
 863 suggest that sub-band wavelet descriptors would be better pixel-based de-
 864 scriptors for scale-saliency computation. In terms of NSS, QWT has slightly
 865 out-performed the other descriptors, and its value nearly approaches NSS
 866 result of ITT and obviously surpasses PSS's result.

867 The graph 9 and the table 4 shows numeric evaluation of the proposed
 868 methods with WSS scale section mechanism on Kootstra's database. Besides
 869 WSS scale selection, we have another method called DIS; therefore, we should
 870 compare how DIS performs on the same database with suggested sub-band
 871 descriptors. Therefore, similar quantitative assessments are also done for
 872 wavelet scale saliency with DIS scale selection and simulation results are
 873 shown in figure 10 and table 5.

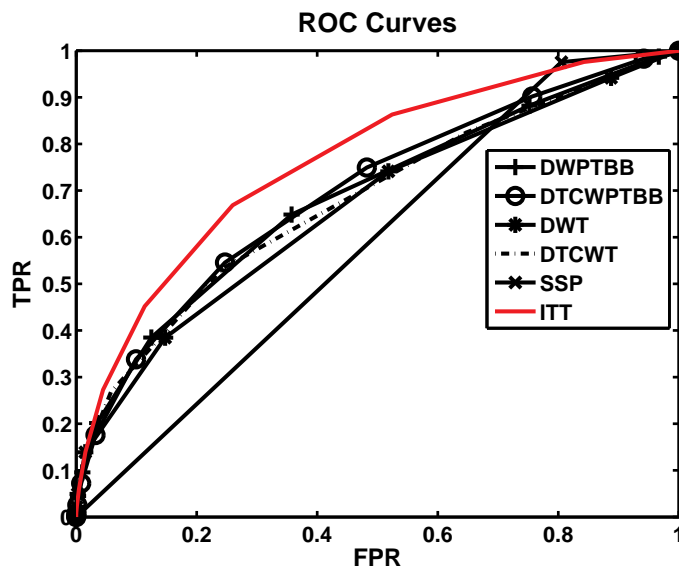


Figure 10: ROC Curve - DIS

874 With this specific simulation parameters, the method still performs quite
 875 well against other methods like ITT and PSS in both terms of AUC and

MTH	AUC	NSS	TIME(s)
ITT	0.7819	0.5144	2.3874
PSS	0.5852	-0.3532	17.0663
DWT	0.7058	0.4847	0.4169
DTCWT	0.7173	0.5027	2.8972
DWPTBB	0.7173	0.4556	4.8156
DTCWPTBB	0.7381	0.3468	4.7152

Table 5: Quantitative Result

876 NSS. However, both AUC and NSS of DIS are slightly worse than those of
877 DIS methods. Noteworthy, ITT analyses three channels color, intensity and
878 orientation simultaneously while we just utilize a intensity channel. Only
879 one channel is chosen since we try to isolate the performance of wavelet scale
880 saliency from other external effects such richness of input features. Regardless
881 of DIS or WSS, the method has very competitive results in numeric terms
882 and it is not due to comprehensiveness of input features.

883 8.3. Qualitative Comparison of Saliency Methods

884 In this section, we show a few examples of visual saliency maps from two
885 mentioned database of Bruce and Kootstra. From each of the databases,
886 only four test images are chosen to be displayed due to limited space though
887 saliency maps are generated for every single image in either of the databases.
888 The samples are intentionally chosen to show variety of contexts and scenes
889 as well as they cover cases of successfully highlighting interested objects
890 and cases of failing to emphasize salient regions. Along with the proposed
891 methods, saliency-maps of ITT and PSS methods are also included so as to
892 give visual comparisons to our proposed saliency methods. Directly below
893 are displayed four samples from Neil Bruce’s database.

894 There are four samples , shown in figures 11,12,13,14, for qualitatively
895 analysing. Generally, PSS identifies a large portion of images as salient re-
896 gions (white regions), it explains why its average AUC and NSS in the table
897 2 are the lowest, and ITT model gives reasonable saliency maps for three
898 over four samples. Four samples of saliency maps are deliberately chosen to
899 show that different ranking of WSS, DIS derivatives, and their dependence
900 on mother wavelet morphological shapes. Sometimes, their performances
901 are quite similar, the figure 11; however, QWT-WSS performs better than
902 DWT-WSS in many samples; for example, figure 7. DWPTBB-WSS and

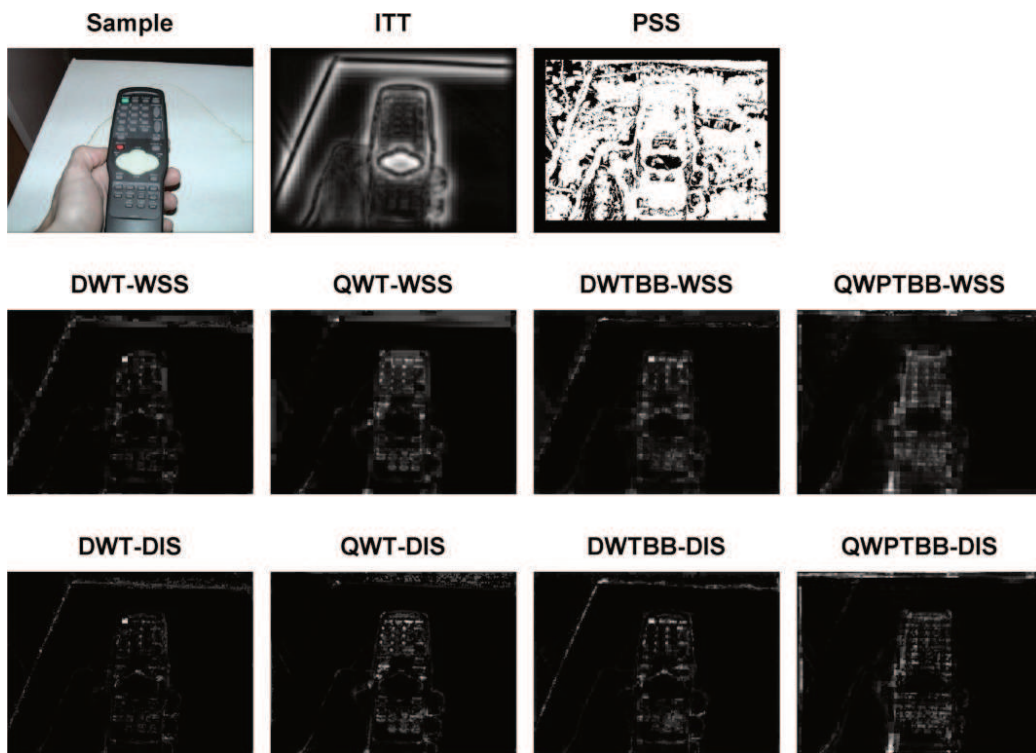


Figure 11: Saliency Map 1

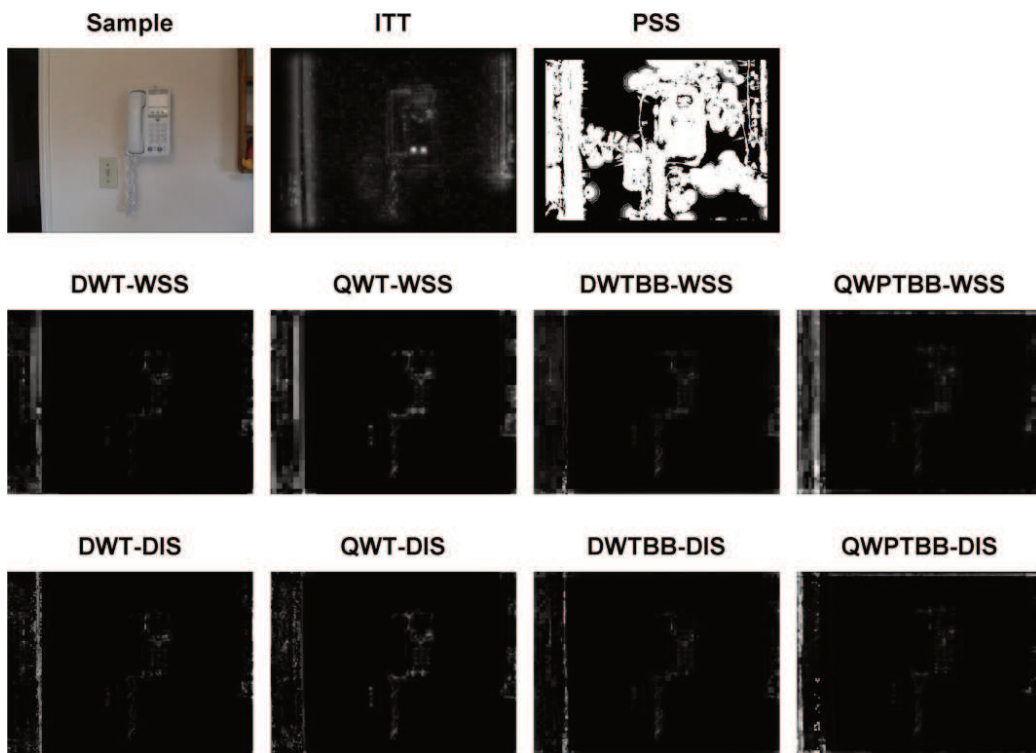


Figure 12: Saliency Map 2

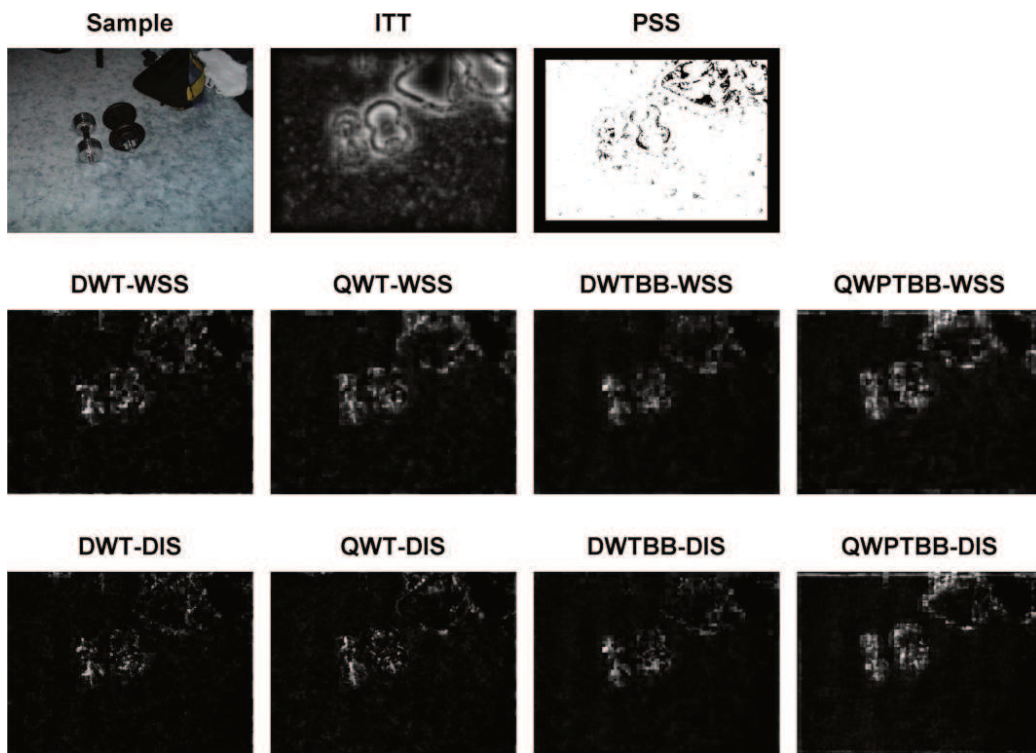


Figure 13: Saliency Map 3

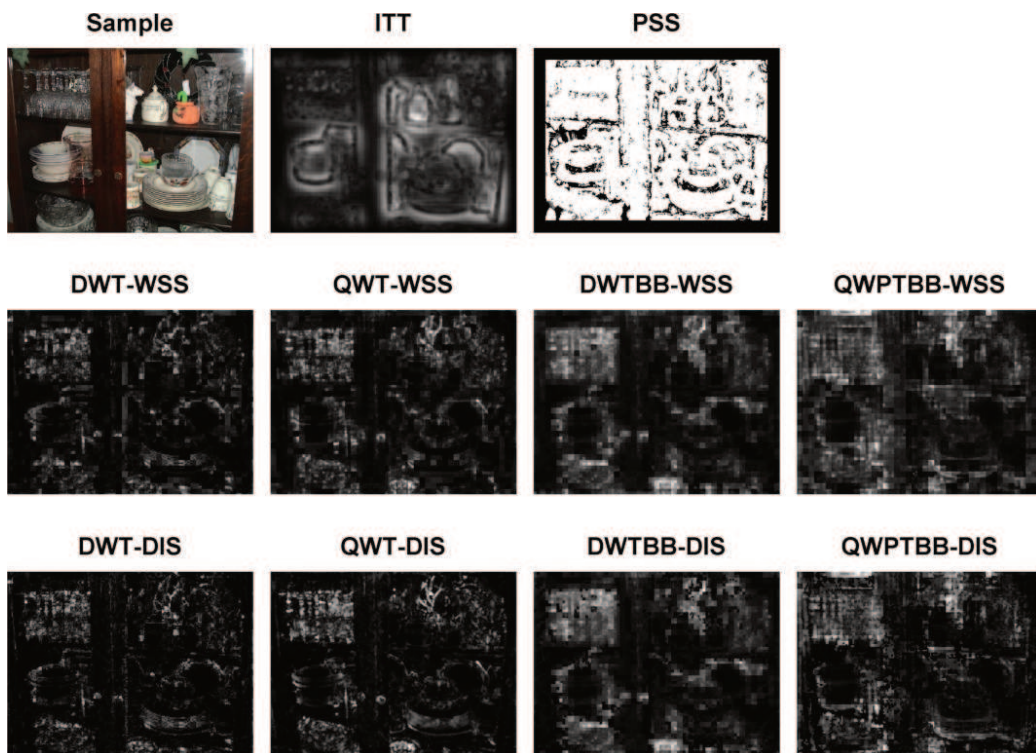


Figure 14: Saliency Map 4

903 QWPTBB-WSS also have their own advantages, especially in the case tex-
 904 tured background - figure 13. Finally, sometimes none of proposed methods
 905 do give reasonable saliency maps, figure 14. It usually happens if images are
 906 flooded with complex textures.

907 While Neil Bruce’s data-set capture daily scenes in the urban and subur-
 908 ban areas, it lacks of scenes from natural landscapes. Therefore, its images
 909 do not represent the whole meaning of ”natural images” category. In order
 910 to visually confirm effectiveness of our proposed methods, we include four
 911 ”natural” samples with corresponding saliency maps from the Kootstra’s
 912 database in the following figures 15, 16, 17 and 18.

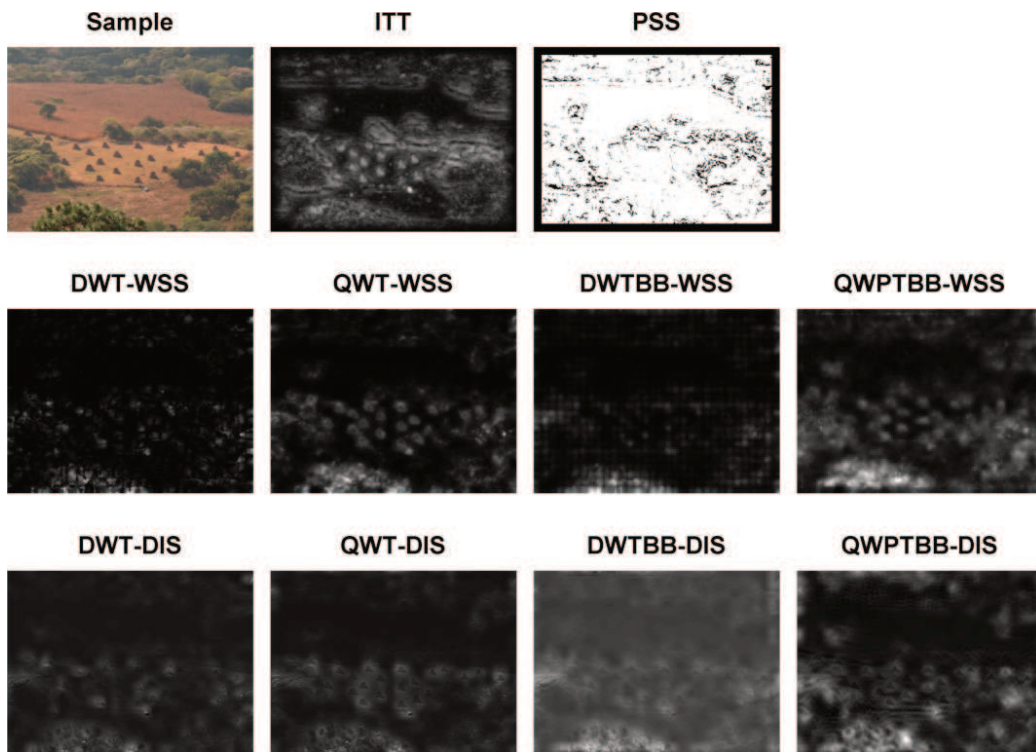


Figure 15: Saliency Map 1

913 In accordance with one sample image (in color), we display saliency maps
 914 produced by ITT , PSS , and eight derivatives of the proposed wavelet scale
 915 saliency methods. The figures 15 and 18 represents image of flowers taken in
 916 close distance. Therefore, it shows quite a number of symmetric and small
 917 details. Meanwhile, figures 16 and 17 contains the whole landscape of moun-

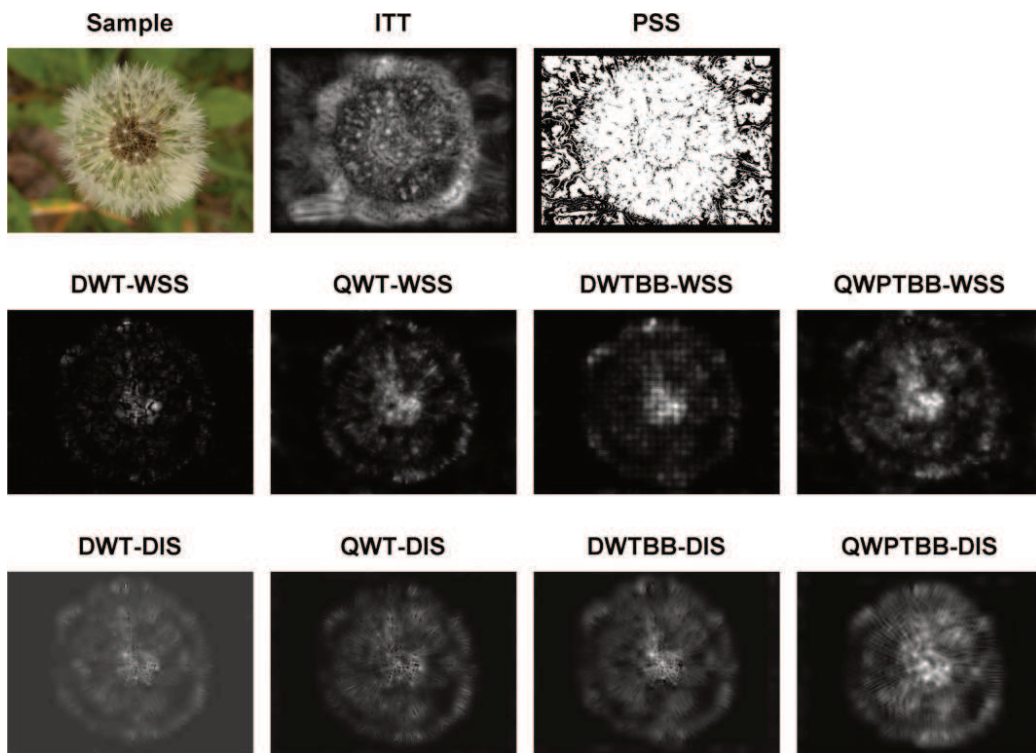


Figure 16: Saliency Map 2

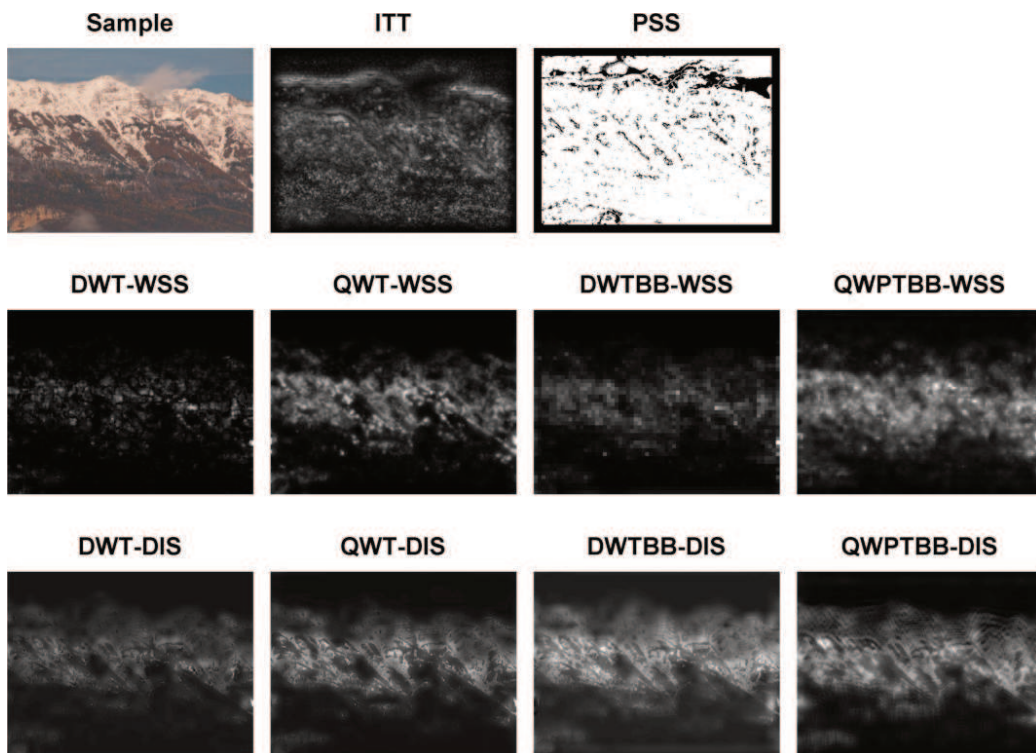


Figure 17: Saliency Map 3

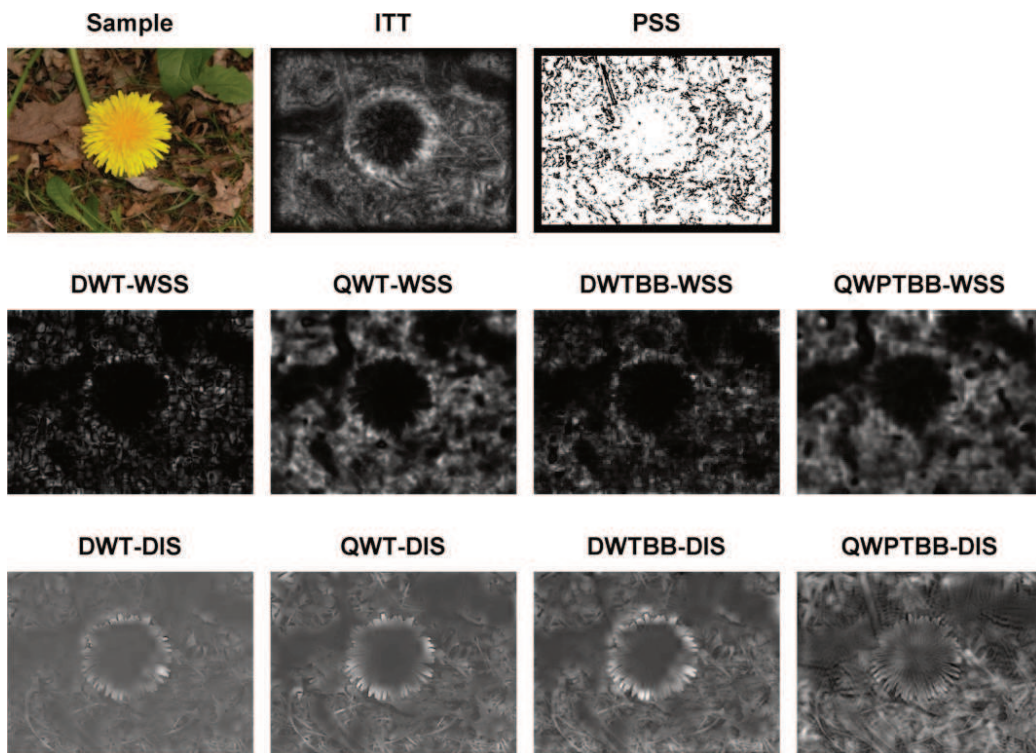


Figure 18: Saliency Map 4

918 tains and plateaus. Those scenes are usually anti-symmetric and much richer
919 in information than flowery photos. In general observations, ITT method
920 does the best job in selecting the salient features. Among derivatives of the
921 proposed features, QWPTBB descriptors show the most competitive and
922 comprehensive visual result, followed by QWT, DWTBB, and DWT based
923 derivatives in descending order of performances. For comparison between
924 WSS and DIS scale-selection mechanisms, there is slight but significant dif-
925 ference between their saliency maps - WSS saliency maps in the second rows
926 and DIS saliency maps in the third rows of the figures 15,16,17, and 18. In
927 these examples, DIS maps tend to highlight more features than those of WSS;
928 in other words, WSS maps might have better discriminant power than DIS
929 maps. It would explain why AUC and NSS results in the table 4 are slight
930 better than those in the table 5. There are small changes in quantitatively
931 visual results when different parameters are used. However, the proposed
932 methods performs very well against other saliency methods like ITT and
933 PSS.

934 **9. Conclusion**

935 In this paper, we propose the extension of scale saliency from pixel de-
936 scriptors to sub-band energy density descriptors generated by four DWT,
937 DWPTBB, QWT, and QWPTBB wavelet transforms with two different scale
938 selection mechanisms WSS and DIS. Comparing to pixel-value descriptors
939 (PSS), the proposed descriptors are much more sparse but biased toward
940 morphological shapes of mother wavelet. Moreover, the proposed descriptors
941 are more robust to external influencing factors to generation of saliency maps
942 such as shift-variance and other affine transformation. Furthermore, wavelet
943 packet descriptors with best basis algorithms are also considered since several
944 psychological experiments suggest sparseness factor in human vision system.
945 Along with new descriptors, innovative coherent information framework for
946 wavelet scale saliency is proposed and strong relations with Bayesian Sur-
947 prise Model [14] are emphasized. Beside solid theoretical development, the
948 experimental results are as well competitive with state-of-the-art ITT model
949 and surpasses the original scale saliency model PSS quantitatively and qual-
950 itatively. In future research, theoretical analysis will be extended to include
951 prior information or top-down information, perceptual grouping and other
952 visual attention operations.

953 **References**

- 954 [1] U. Neisser, *Cognitive Psychology*, 4319, Appleton-Century-Crofts, 1967.
- 955 [2] David Marr, *Vision: A Computational Investigation into the human*
956 *representation and processing of visual information*, Inc, New York, NY,
957 1982.
- 958 [3] L. Itti, C. Koch, E. Niebur, Others, A model of saliency-based visual at-
959 *tention for rapid scene analysis*, *IEEE Transactions on pattern analysis*
960 *and machine intelligence* 20 (1998) 1254–1259.
- 961 [4] D. Walther, *Interactions of Visual Attention and Object Recognition:*
962 *Computational Modeling, Algorithms, and Psychophysics*, *interactions*
963 2006 (2006).
- 964 [5] J. Harel, C. Koch, P. Perona, *Graph-based visual saliency*, *Advances in*
965 *neural information processing systems* 19 (2007) 545.
- 966 [6] X. Hou, L. Zhang, *Saliency detection: A spectral residual approach*,
967 *in: IEEE Conference on Computer Vision and Pattern Recognition*
968 *(CVPR07)*. IEEE Computer Society, 800, Citeseer, 2007, pp. 1–8.
- 969 [7] T. Kadir, M. Brady, *Saliency, scale and image description*, *International*
970 *Journal of Computer Vision* 45 (2001) 83–105.
- 971 [8] S. Gilles., *Robust Description and Matching of Images*, Ph.D. thesis,
972 University of Oxford, 1998.
- 973 [9] N. Bruce, J. Tsotsos, *Saliency based on information maximization*, *Ad-*
974 *vances in neural information processing systems* 18 (2006) 155.
- 975 [10] D. Gao, V. Mahadevan, N. Vasconcelos, *The discriminant center-*
976 *surround hypothesis for bottom-up saliency*, *Advances in Neural In-*
977 *formation Processing Systems* 20 (2007) 1–8.
- 978 [11] L. N. Anh Cat, G. Qiu, U. Geoff, A. Li-minn, S. Kah Phooi, *Visual*
979 *Information Based on Fast nonparametric multidimensional entropy es-*
980 *timation*, *International Conference on Acoustic, Speed and Signal Pro-*
981 *cessing* (2012).

- 982 [12] G. Qiu, X. Gu, Z. Chen, Q. Chen, C. Wang, An information theoretic
983 model of spatiotemporal visual saliency, in: international conference on
984 multimedia and expo, Citeseer, 2007, pp. 1806–1809.
- 985 [13] T. Kadir, D. Boukerroui, M. Brady, An analysis of the scale saliency
986 algorithm, OUEL No: 2264 3 (2003) 1–38.
- 987 [14] P. Baldi, L. Itti, Of bits and wows: A Bayesian theory of surprise with
988 applications to attention., *Neural networks : the official journal of the*
989 *International Neural Network Society* 23 (2010) 649–66.
- 990 [15] N. D. B. Bruce, J. K. Tsotsos, Saliency , attention , and visual search :
991 An information theoretic approach, *Journal of Vision* 9 (2009) 1–24.
- 992 [16] G. Kootstra, B. de Boer, L. R. B. Schomaker, Predicting Eye Fixations
993 on Complex Visual Stimuli Using Local Symmetry., *Cognitive compu-*
994 *tation* 3 (2011) 223–240.
- 995 [17] J. Starck, F. Murtagh, Multiscale entropy filtering, *Signal Processing*
996 76 (1999).
- 997 [18] P. Suau, F. Escolano, A new feasible approach to multi-dimensional
998 scale saliency, in: *Advanced Concepts for Intelligent Vision Systems*,
999 Springer, 2009, pp. 77–88.
- 1000 [19] D. Stowell, M. D. Plumbley, Fast multidimensional entropy estimation
1001 by k-d partitioning, *Signal Processing* 16 (2009) 537–540.
- 1002 [20] C. Koch, S. Ullman, Shifts in selective visual attention: towards the
1003 underlying neural circuitry, *Hum Neurobiol* 4 (1985) 219–227.
- 1004 [21] F. Urban, B. Follet, C. Chamaret, O. Meur, T. Baccino, Medium Spatial
1005 Frequencies, a Strong Predictor of Saliency, *Cognitive Computation*
1006 (2010).
- 1007 [22] A. B. Watson, The cortex transform: Rapid computation of simulated
1008 neural images, *Computer Vision, Graphics, and Image Processing* 39
1009 (1987) 311–327.

- 1010 [23] H. Senane, A. Saadane, D. Barba, Image coding in the context of a psy-
1011 chovisual image representation with vector quantization, in: Proceed-
1012 ings., International Conference on Image Processing, volume 1, IEEE
1013 Comput. Soc. Press, 1995, pp. 97–100.
- 1014 [24] M. Unser, N. Chenouard, D. Van de Ville, Steerable pyramids and tight
1015 wavelet frames in $L_2(\mathbb{R}(d))$., IEEE transactions on image processing :
1016 a publication of the IEEE Signal Processing Society 20 (2011) 2705–21.
- 1017 [25] M. N. Do, M. Vetterli, The contourlet transform: an efficient directional
1018 multiresolution image representation., IEEE transactions on image pro-
1019 cessing : a publication of the IEEE Signal Processing Society 14 (2005)
1020 2091–106.
- 1021 [26] W. L. Chan, H. Choi, R. G. Baraniuk, Coherent multiscale image pro-
1022 cessing using dual-tree quaternion wavelets., IEEE transactions on im-
1023 age processing : a publication of the IEEE Signal Processing Society 17
1024 (2008) 1069–82.
- 1025 [27] S. Mallat, A wavelet tour of signal processing, 2, Academic Pr, 1999.
- 1026 [28] R. R. Coifman, M. V. M. Wickerhauser, Entropy-Based Algorithms
1027 for Best Basis Selection, IEEE Transactions on Information Theory 38
1028 (1992) 713–718.
- 1029 [29] T. Bulow, G. Sommer, Hypercomplex signals-a novel extension of the
1030 analytic signal to the multidimensional case, IEEE Transactions on
1031 Signal Processing 49 (2001) 2844 –2852.
- 1032 [30] N. Kingsbury, The dual-tree complex wavelet transform: a new tech-
1033 nique for shift invariance and directional filters, Proc. 8th IEEE DSP
1034 Workshop (1998) 2–5.
- 1035 [31] N. Kingsbury, Complex wavelets for shift invariant analysis and filtering
1036 of signals, Applied and Computational Harmonic Analysis 10 (2001)
1037 234–253.
- 1038 [32] I. Bayram, On the Dual-Tree Complex Wavelet Packet and M-Band
1039 Transforms, Processing, IEEE Transactions on (2008) 1–27.

- 1040 [33] I. Cohen, S. Raz, D. Malah, Orthonormal shift-invariant wavelet packet
1041 decomposition and representation, *Signal Processing* 57 (1997) 251–270.
- 1042 [34] Z. Azimifar, M. Amiri, P. Fieguth, E. Jernigan, Empirical Study of
1043 Wavelet Domain Image Joint Statistics and Proposition of an Efficient
1044 Correlation Map, *Journal of Mathematical Imaging and Vision* (2011).
- 1045 [35] I. Selesnick, R. Baraniuk, N. Kingsbury, The dual-tree complex wavelet
1046 transform, *IEEE Signal Processing Magazine* 22 (2005) 123–151.
- 1047 [36] R. Buccigrossi, E. Simoncelli, Image compression via joint statistical
1048 characterization in the wavelet domain, *IEEE Transactions on Image*
1049 *Processing* 8 (1999) 1688–1701.
- 1050 [37] A. Borji, D. N. Sihite, L. Itti, Quantitative Analysis of Human-Model
1051 Agreement in Visual Saliency Modeling: A Comparative Study., *IEEE*
1052 *transactions on image processing* : a publication of the IEEE Signal
1053 *Processing Society PP* (2012) 1.